



GPS Measurements of Precipitable Water Vapor Can Improve Survey Calibration: A Demonstration from KPNO and the Mayall z -band Legacy Survey

W. M. Wood-Vasey¹ , Daniel Perrefort^{1,2} , and Ashley D. Baker^{3,4} ¹ Pittsburgh Particle Physics, Astrophysics, and Cosmology Center (PITT PACC), Physics and Astronomy Department, University of Pittsburgh, Pittsburgh, PA 15260, USA² Center for Research Computing, University of Pittsburgh, Pittsburgh, PA 15260, USA³ University of Pennsylvania Department of Physics and Astronomy, 209 S 33rd Street, Philadelphia, PA 19104, USA⁴ Department of Astronomy, California Institute of Technology, Pasadena, CA 91125, USA

Received 2020 October 26; revised 2022 March 31; accepted 2022 April 1; published 2022 May 20

Abstract

Dual-band Global Positioning Satellite (GPS) measurements of precipitable water vapor (PWV) at the Kitt Peak National Observatory predict the overall per-image sensitivity of the Mayall z -band Legacy Survey (MzLS). The per-image variation in the brightness of individual stars is strongly correlated with the measured PWV and the color of the star. Synthetic stellar spectra through TAPAS transmission models successfully predict the observed PWV-induced photometric variation. We find that PWV absorption can be well approximated by a linear relationship with $(\text{airmass} \times \text{PWV})^{0.6}$ and present an update on the traditional treatment in the literature. The MzLS zero-point sensitivity in electrons s^{-1} varies with a normalized-mean absolute deviation of 61 mmag. PWV variation accounts 23 mmag of this zero-point variation. The MzLS per-image absolute sensitivity decreases by 40 mmag per effective mm of PWV. The overall gray offset portion of this variation is corrected by the calibration to a reference catalog. But the relative calibration error between blue ($r - z < 0.5$ mag) versus red ($1.2 \text{ mag} < r - z$) stars increases by 0.3–2 mmag per effective mm of PWV. We argue that GPS systems provide more precise PWV measurements than using differential measurements of stars of different colors and recommend that observatories install dual-band GPS as a low-maintenance, low-cost, auxiliary calibration system. We extend our results of the need for well-calibrated PWV measurements by presenting the calculations of the PWV photometric impact on three science cases of interest: stellar photometry, supernova cosmology, and quasar identification and variability.

Unified Astronomy Thesaurus concepts: Earth atmosphere (437); Flux calibration (544); Water vapor (1791); Astronomical methods (1043); Sky surveys (1464); Exoplanet detection methods (489); Type Ia supernovae (1728); Observational cosmology (1146); Quasars (1319)

1. Introduction

Modern astronomical surveys such as the Dark Energy Survey (DES; Dark Energy Survey Collaboration et al. 2016) and the Panoramic Survey Telescope and Rapid Response System (Pan-STARRS; Magnier et al. 2020) require high photometric accuracy and precision. Upcoming surveys such as the Vera Rubin Observatory Legacy Survey of Space and Time (LSST; Ivezić et al. 2019) will strive to push this limit even further by requiring a 5 mmag photometric precision with an absolute calibration of 10 mmag. For surveys relying on ground-based telescopes, accounting and correcting for effects induced by the Earth’s atmosphere is a key step in achieving this goal (see Ivezić et al. 2007; Burke et al. 2010, 2014, 2018; Magnier et al. 2020). In particular, absorption features due to the presence of water vapor dominate the atmospheric transmission function in the red optical and near-infrared (NIR) bandpass ($\lambda > 550$ nm). The complicated yet known structure of water vapor absorption must be accurately and precisely accounted for to accurately determine the complete system throughput as a function of wavelength.

Broadband imaging is traditionally calibrated using a reference catalog to compute correction terms for color,

airmass, and a higher-order color-airmass term. While this approach implicitly corrects for first-order effects introduced by the atmospheric opacity, it does not account for second-order effects caused by differences in the atmospheric absorption between the spectral energy distributions (SEDs) of the target and reference stars. Because redder stars emit much more of their light at wavelengths susceptible to atmospheric absorption, their photometric values vary differently than bluer stars with changes in atmospheric conditions. This difference in behavior can introduce second-order photometric errors of over 1% (Ivezić et al. 2007; Li et al. 2016), which is significant in an era of high-precision photometry.

Approaches that allow for time-dependent color terms can account for time-variable absorption. These color terms work best where the differences in the SEDs can be described by smooth monotonic functions, such as in the Rayleigh–Jeans tail of the effective blackbody approximation for K-type and hotter stars. This approach works particularly well for effects that themselves are smooth in wavelength, such as Mie scattering due to atmospheric aerosols. However, the contribution to the atmospheric absorption due to atmospheric water vapor is not smooth.

Unlike the attenuation of light due to ozone and aerosols, absorption due to precipitable water vapor (PWV) has a complex transmission function with lines that saturate even during relatively dry and *photometric* conditions ($\text{PWV} \approx 5$ mm). The convention is to measure water vapor in units of the mm of liquid water if it were all condensed. Local PWV concentrations can



Original content from this work may be used under the terms of the [Creative Commons Attribution 4.0 licence](https://creativecommons.org/licenses/by/4.0/). Any further distribution of this work must maintain attribution to the author(s) and the title of the work, journal citation and DOI.

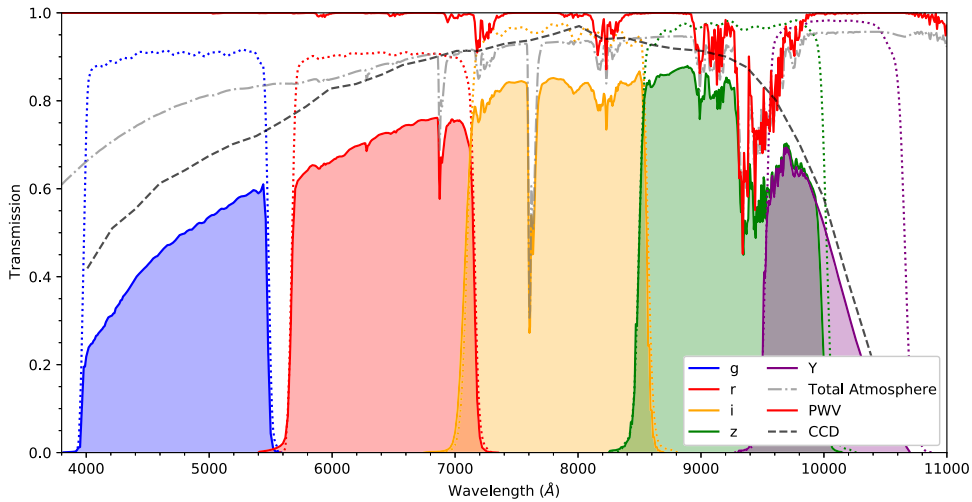


Figure 1. The optical throughput of DECam in the *grizY* bandpasses. The same type of LBNL 500 μm thick CCDs were used for both DECam and Mosaic3, and the *z*-band filter used for MzLS is the same design as the DECam filter. The quantum efficiency response of the CCD (dashed black) shows the red-optimized nature of these CCDs. A characteristic atmosphere (gray dashed-dotted) shows the smooth effects of Rayleigh and Mie scattering, the narrow absorption lines in *r* and *i* due to O_2 , and the significant structure of PWV. This line also includes the smoother effects from O_3 , which can be seen as a small depression from 5500–6500 Å. The Rayleigh scattering and O_2 absorption are stable and well understood, while O_3 , Mie scattering due to aerosols, and PWV have significant time variability. We explicitly emphasize the absorption structure due to PWV with an additional line (solid red) for $\text{PWV} \approx 4$ mm to highlight the key source of absorption for this present work. In *z* band, PWV is the dominant atmospheric absorber. The *i*-band transmission is also affected by PWV absorption, but the effect is a significantly smaller fraction of the atmospheric transmission.

change by up to 10% per hour (Thomas-Osip et al. 2010; Li et al. 2017), requiring a photometric correction that varies over the course of an observing night. Correctly accounting for variable complex atmospheric transmission requires a detailed understanding of the atmospheric state during the time in which observations were performed.

A common astronomical method for quantifying the absorption due to the atmosphere is to perform dedicated observations of a young A-type star (e.g., as in Stubbs et al. 2007). Because these stars have relatively few intrinsic features and are well described by existing models, the effects of atmospheric absorption can be fit for using forward modeling. When performed spectroscopically, fitting these observations provides a detailed map of the per-wavelength transmission of the atmosphere. This approach can also be performed photometrically by using narrowband filters centered on key atmospheric features (Li et al. 2014; Baker et al. 2017). This narrowband image approach benefits from the ability to perform in situ measurements along a similar line of sight to the scientific observations. Both of these approaches require the maintenance and calibration of a secondary, dedicated telescope.

An alternative method to measure the water absorption is to use dual-band receivers tracking signals from Global Positioning Satellites (GPS). By measuring the delay of dual-band GPS signals traveling through the atmosphere, it is possible to determine the PWV column density along zenith (Nahmias & Zabransky 2004; Blake & Shaw 2011; Manandhar et al. 2018). Through the use of atmospheric models and scaling relations, the atmospheric transmission due to PWV can be determined for the line-of-sight airmass of a given observation. This approach benefits from the ability to perform atmospheric measurements in near real-time and results in values that correlate strongly with spectroscopic measurements (Li et al. 2017). However, GPS measurements tend to be less accurate in dry conditions (Buehler et al. 2012; Hagemann et al. 2003) and

cannot constrain the transmission due to secondary (non-PWV) components of the atmosphere.

In this work, we demonstrate the effect of PWV on the measured per-image zero-points and per-object color-dependent per-image offsets using observations taken by the Mayall *z*-band Legacy Survey (MzLS) combined with contemporaneous GPS PWV measurements from Kitt Peak National Observatory (KPNO).

In Section 2, we outline the MzLS observations (2.1), PWV measurements (2.2), and atmospheric models (2.3) considered by this work. In Section 3, we demonstrate the effects of PWV absorption on MzLS zero-points and compare using GPS-measured PWV to using the differential brightness of stars of different colors to predict zero-point variation. We then consider the impact of PWV on various science cases in Section 5, including the impact on stars (5.1), supernovae (5.2), and quasars (5.3). Finally, we discuss the application of PWV measurement techniques to upcoming surveys in Section 6.

2. Data

2.1. Mayall *z*-band Legacy Survey

The Mayall *z*-band Legacy Survey (MzLS) is one of the three public surveys that comprised the DESI Legacy Imaging Surveys⁵ (Dey et al. 2019). Using the Mosaic3 camera on the 4 meter Mayall telescope at KPNO (Dey & Valdes 2014; Dey et al. 2016), MzLS observed approximately 5, 100 deg^2 of the sky in the *z* band. Mosaic3 represents a significant upgrade from the Mosaic1 and Mosaic2 cameras (Dey & Valdes 2014), with a 500 μm thick CCD that significantly increased the quantum efficiency out to $\lambda = 1$ μm . The *z*-band Mosaic3 filter, shown in Figure 1, was chosen to be very similar to the *z*-band filter of the Dark Energy Camera (DECam; Flaugher et al. 2015) on the CTIO 4 meter Blanco telescope to allow for standard comparisons across hemispheres. After a

⁵ <http://legacysurvey.org>

commissioning phase for Mosaic3 from 2015 October–December, the MzLS survey formally ran from 2016 February 2 through 2018 February 12. There are 60,431 exposures recorded in the MzLS archive, with 60,403 exposures with a nonzero recorded zero-point.

In order to increase the observable depth, MzLS used a 3-pass strategy to tile the sky (Burleigh et al. 2020). To ensure the accurate calibration of each exposure, the first pass of observations was performed exclusively when both of two conditions were met: clear skies with a transparency $\geq 90\%$, and a seeing better than $1''.3$. The second pass was performed when at least one of these conditions were met, and the third pass was performed with no requirements. This approach guaranteed at least one high-quality observation at each location in the sky that can be used to calibrate the photometry across the entire survey footprint.

MzLS observations taken during the second and third passes were calibrated by directly matching to overlapping observations taken during the first pass. The zero-points were then determined individually for each CCD by measuring the instrumental magnitude of each source and matching the source to photometry from the first Pan-STARRS data release (PS1 DR1; Schlafly et al. 2012).

To facilitate this comparison, a subset of PS1 DR1 sources were selected as calibrators and their colors were compared empirically to create a map between the PS1 and MzLS instrumental systems (Dey et al. 2019, Equation (6)). Thus while the MzLS natural system itself is absolutely calibrated to PS1, the individual image-by-image zero-points are in the MzLS natural system. The reported zero-point is defined as the magnitude of a source that generate one count per second.⁶ See Section 3.2 for a more detailed investigation on the reported zero-points.

2.2. Precipitable Water Vapor

In 2015 March, we installed a dual-band GPS receiver on the WIYN 3.5 meter telescope building at KPNO to monitor the local PWV column density (Perrefort et al. 2019). Estimation of the PWV concentration from the resulting meteorological data is provided by the SuomiNet project (Ware et al. 2000). With the addition of pressure, temperature, and relative humidity measurements, SuomiNet estimates the PWV column density at zenith by measuring the delay of dual-band GPS signals traveling through the atmosphere. For KPNO, these values are compiled by SuomiNet at thirty-minute intervals.

The application of GPS receivers to monitor PWV works by measuring the relative phase shift between two GPS frequencies emitted through the atmosphere (for details on the methods, see Bevis et al. 1994, 1992). The magnitude of the delay imposed on each signal is directly related to the frequency-dependent index of refraction along the optical path. This delay, known as the Zenith Total Delay, can be separated into a wet (PWV driven) and dry (non-PWV) component through the use of atmospheric models (Tralli & Lichten 1990). Although this approach is a recent advent in astronomy (Braun & Hove 2005; Dumont & Zabransky 2001; Nahmias & Zabransky 2004; Blake & Shaw 2011), the use of GPS to measure PWV has a longer history in meteorology (Bevis et al. 1992) and has undergone continual improvement with a focus on minimizing the estimated uncertainty, often achieving levels

Table 1
MzLS Exposure Counting

Set	Exposures
MzLS Survey + Commissioning	60,431
MzLS Survey	58,140
MzLS Survey in 2016A, 2017A, 2017B	55,479
25.75 < zero point < 26.75 mag	55,277
“Clean”: 25.75 < zero point < 26.75 mag in 2016A, 2017A, 2017B	52,709

≤ 2 mm (Moore et al. 2015; Shanguan et al. 2015; Sapucci et al. 2019).

From 2016 January through March, the barometric sensor at the KPNO WIYN 3.5 m weather station malfunctioned intermittently. This caused successive nonphysical spikes in PWV estimates measured during this period. During these times we used estimates of the KPNO PWV based on the nearby dual-band GPS monitor stations—see Perrefort et al. (2019) for details. Table 1 details the number of exposures for subsets of the MzLS survey relevant for this work. Figure 2 shows the distribution of airmass, MJD, and zero-point for the MzLS survey along with the PWV_{zenith} values measured from the KPNO dual-band GPS. PWV_{zenith} values are comparable across the seasons, although 2017B started with a particularly high PWV_{zenith} during the monsoon season. However, the airmass values in the 2017B season were significantly higher because the MzLS region extends from $100 < \text{R.A.} < 300$ degrees and so observations made in the second half of the year had to reach over farther from zenith to access the MzLS region. Once the full MzLS region became more visible in the last part of 2017B, the airmass of the observations came back down.

2.3. Telluric Transmission Models

To model telluric water vapor absorption, Rayleigh, and Mie scattering, we use the TAPAS web service (Bertaux et al. 2014) to generate the atmospheric transmission function for KPNO at an airmass of 1 assuming the average latitude winter model. Bertaux et al. (2014) do not specify the scattering function assumed for their Rayleigh scattering model, but all model spectra assume average atmospheric conditions appropriate for the latitude, longitude, and elevation of Kitt Peak Observatory, which is sufficient for this study. When referring to an airmass of 1, we mean with respect to the elevation of the observing site, which in this work is taken to be KPNO.

Figure 3 shows the extracted PWV component of atmospheric absorption for water vapor transmission model with 1, 5, and 10 mm values of PWV. The PWV band has significant effects in the redder half of the MzLS z -band filter. We also show the percentage of saturated lines to illustrate the nonlinearity of the scaling of the absorption as lines saturate.

3. Results from MzLS

We here analyze the dependency of the MzLS zero-points on and per-epoch variations in inferred magnitudes of stars as a function of their color and PWV. Section 3.2 describes standardizing the zero-points to be in $e^- s^{-1}$. Section 3.3 investigates the MzLS zero-point variation with MJD. Section 3.4 presents that the majority of the remaining zero-point variation is well explained by the GPS-measured PWV at KPNO. Section 3.5 examines the per-epoch observations of

⁶ <https://www.legacysurvey.org/dr9/files/>

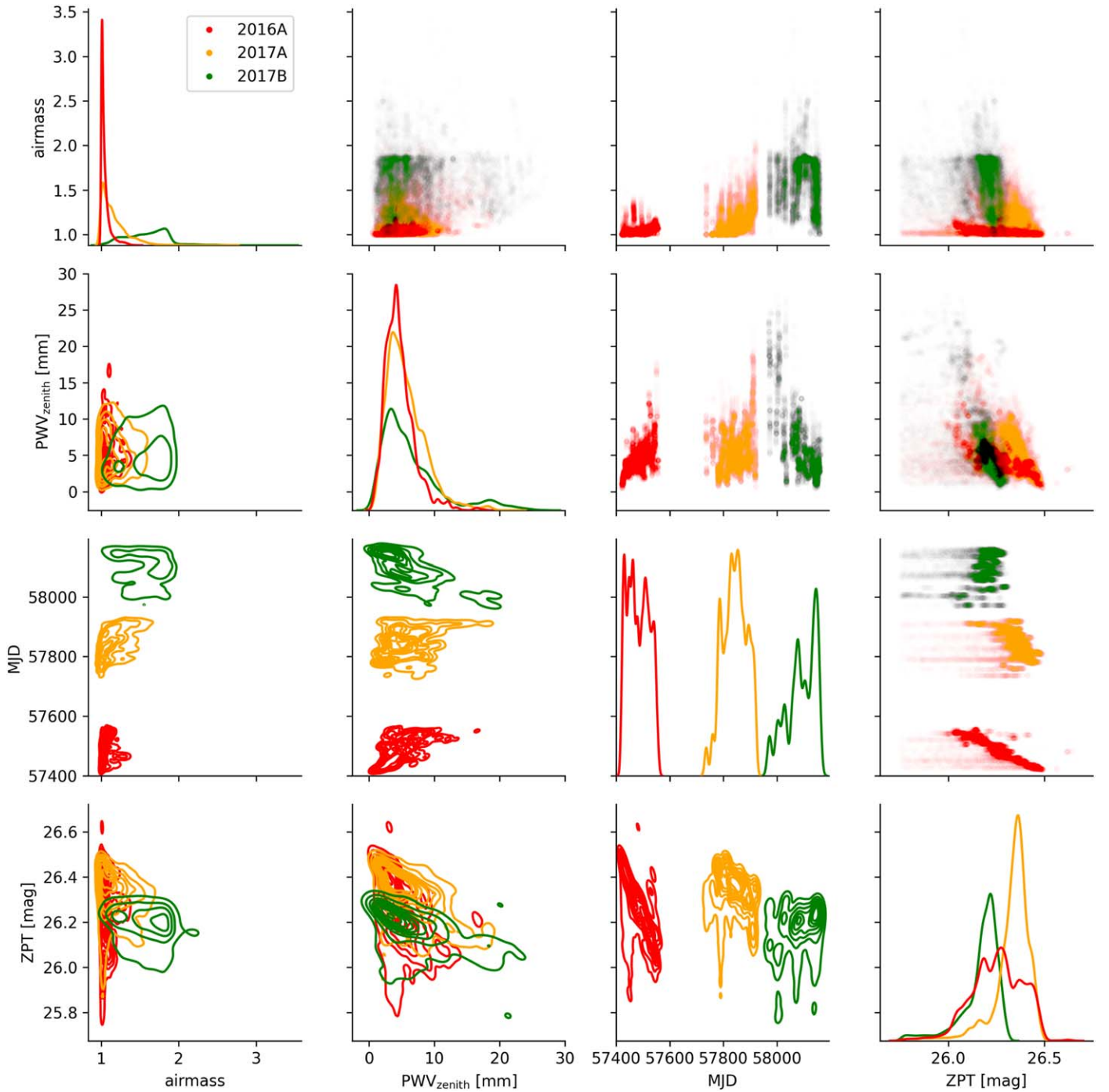


Figure 2. The airmass, $\text{PWV}_{\text{zenith}}$, MJD, and zero-point (in counts s^{-1}) distribution for the MzLS data. The points and lines are color-coded by season: (red) 2016A, (yellow) 2017A, (green) 2017B. The upper right are scatter plots, while the lower left are contours from Gaussian-kernel density estimates. The diagonal plots are normalized-Gaussian-kernel density estimates of that intersecting parameter. Note that the airmass distribution in the last semester of the survey was much wider. The distribution of $\text{PWV}_{\text{zenith}}$ was relatively the same across seasons, but the significantly higher airmass in 2017B means that PWV_{los} was systematically greater for observations in this season.

each star and analyzes the variation in inferred magnitude as a function of stellar color and PWV.

3.1. A Clean Sample of Zero-Points

We define a *clean* sample of zero-points as being only from the 2016A, 2017A, and 2017B semesters. The 2016B semester of the MzLS survey had only 297 observations, and so we ignore it for this work. We further restrict the clean sample as having zero-points between 25.75–26.75 mag. The minimum

cut eliminates the extended tails of lower values of zero-points from images taken in higher-opacity conditions, while the maximum cut eliminates a few outliers at greater than 26.75 mag that are clearly anomalous.

The clean sample of zero-points shows a normalized-median absolute deviation (NMAD)⁷ of 131 mmag in counts s^{-1} .

⁷ NMAD is normalized such that a Gaussian distribution with a $\sigma = 1$ will have a NMAD = 1.

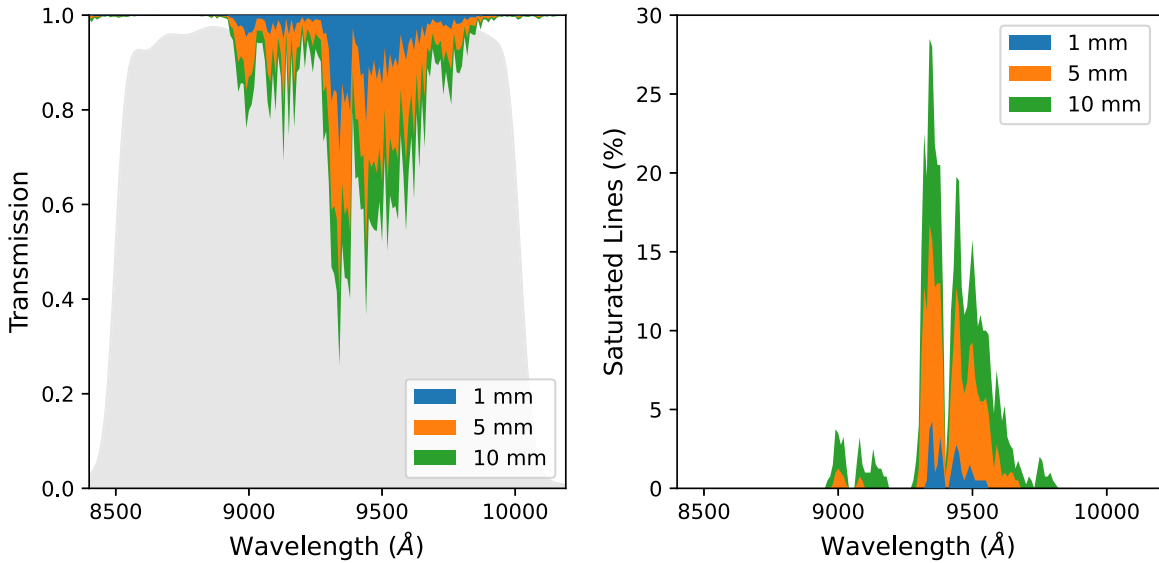


Figure 3. Left: the modeled atmospheric transmission due to PWV for 1 mm (blue), 5 mm (orange), and 10 mm (green) of PWV along line of sight. Gray: the MzLS z -band filter response. As the PWV concentration increases, PWV-absorption lines begin to saturate. Right: percentage of saturated lines as a function of wavelength using a 0.05 nm resolution atmospheric model for each PWV concentration.

3.2. Zero-point, Counts, and Gain

The MzLS zero-points are documented to be in counts s^{-1} . But to analyze the impact of PWV on transmission, what we really want is a measure of the system sensitivity, i.e., the zero-points in photoelectrons s^{-1} [$e^{-} \text{s}^{-1}$]. To convert from counts s^{-1} to $e^{-} \text{s}^{-1}$, one multiplies by the *gain*. The electronic CCD gain values recorded were constant for the MzLS survey: CCD1, 1.94; CCD2, 1.86; CCD3, 1.91; CCD4, 1.72 in units of e^{-}/counts .

But in practice, the effective normalization to $e^{-} \text{s}^{-1}$ is subject to details of the calibration. The images were processed such that they were normalized to close to a gain of 1, i.e., they are almost in photoelectrons s^{-1} across the entire image. The MzLS data processing renormalized the gain between the amps based on the measured sky levels in each amp (Dey et al. 2019, Table 5). Because each CCD has a different gain, this process means that the final calibrated image cannot both be in true $e^{-} \text{s}^{-1}$ for each CCD *and* on the same scale.

But, in principle, as long as the electronic settings did not change, the relative gain *between* the amps should not change. Any such offset due to the different gain values across the CCDs should be fixed and constant throughout the survey. Thus we do not think that the variations in g_{eff} that we discuss in this section are truly *gain* variations in the electronics. Rather we expect that the g_{eff} variations are consequences of choices in the flat-fielding and normalization steps in the processing pipeline.

Counting photons in a CCD exposure is a Poisson process, such that the variance is the same as the mean. So practically, the effective gain is the number that translates counts/image to $\text{photoelectrons/image}$. The “survey-ccds-mosaic-dr9.fits” file from the Legacy Survey’s ninth data release (DR9) provides the “ccdskycounts” and the “skyrms” in counts s^{-1} .

If you scale up the measured ccdskycounts [counts s^{-1}], skycounts/s , and skyrms [counts s^{-1}], $\sigma_{\text{counts/s}}$, by the exposure time of the image, t_{exp} , and then multiply by the effective gain, g_{eff} , to get units of [e^{-}/image], then Poisson statistics says that

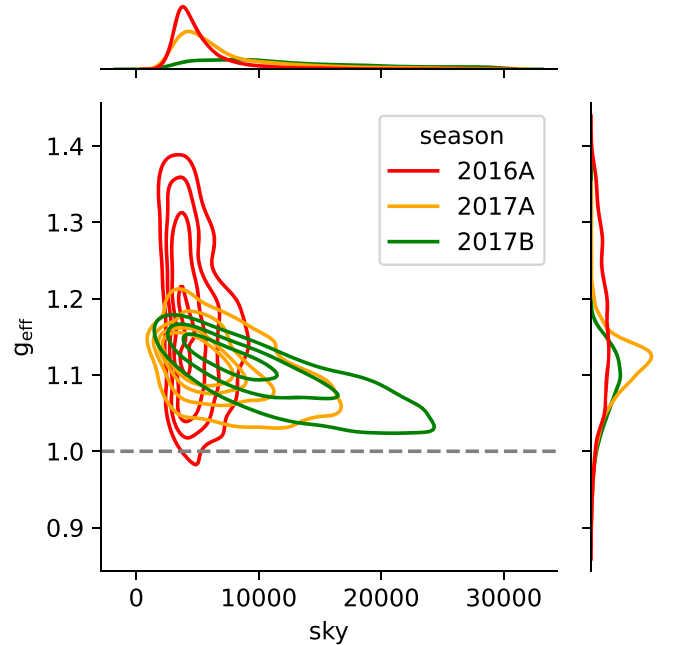


Figure 4. The g_{eff} vs. sky level for each season (2016A: red, 2017A: yellow, 2017B: green). The 2016A season is clearly different than 2017A and 2017B with significant deviation from $g_{\text{eff}} = 1$.

you should have a relationship of

$$\sigma_{e^{-}/\text{image}}^2 = \text{sky}_{e^{-}/\text{image}} \quad (1)$$

$$(g_{\text{eff}} \sigma_{\text{counts/s}} t_{\text{exp}})^2 = g_{\text{eff}} \text{sky}_{\text{counts/s}} t_{\text{exp}} \quad (2)$$

$$g_{\text{eff}} = \frac{\text{sky}_{\text{counts/s}}}{\sigma_{\text{counts/s}}^2 t_{\text{exp}}} \quad (3)$$

The effective gain was in fact close to 1, which would be equivalent to the reported zero-points being in $e^{-} \text{s}^{-1}$. However, it was not explicitly fixed to be 1, and in the 2016A semester, it varied from 0.9–1.4. Figure 4 shows the observed ratio of $\text{ccdskycounts}/\text{skyrms}^2$ versus ccdskycounts .

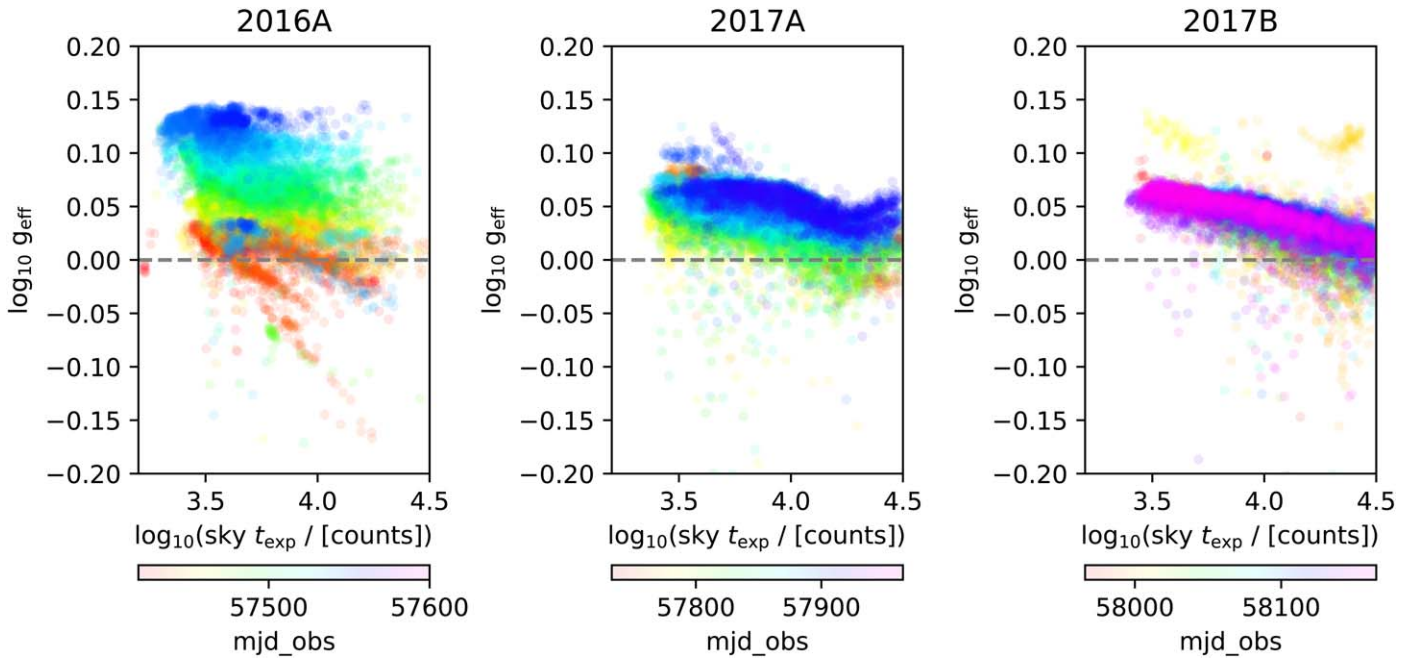


Figure 5. The $\log_{10} g_{\text{eff}}$ vs. \log_{10} sky level in e-/image for each season, color-coded by MJD within each season. Most notably in 2016A, there is a significant constant offset that varies. It is this offset that translates to a change in zero-point. There is also a linear relationship between g_{eff} and \log_{10} sky level, which is not well explained.

There is a clear dependence on the underlying sky level in counts/image.

Figure 5 shows the log-log relationship between g_{eff} and sky level in e-/image. Most notably there are significant changes in g_{eff} in the 2016A season, on the level of almost ~ 0.12 mag. These offsets in log space are equivalent to a multiplicative change in gain. We correct the reported counts s^{-1} zero-points to $e^{-} s^{-1}$:

$$zp_{e^{-}}/s = zp_{\text{counts}/s} + 2.5 \log_{10} g_{\text{eff}}. \quad (4)$$

Thus an offset of $\log_{10} g_{\text{eff}} = 0.12$ translates to a 0.30 mag correction.

There is also a linear relationship between $\log_{10}(g_{\text{eff}})$ and $\log_{10} \text{ccdskycounts}$. This is equivalent to a change in the exponent of 2 in the relationship $g_{\text{eff}} = \text{ccdskycounts}/\text{skyrms}^2$. We do not have a clear explanation for this relationship and do not correct for it.

Figure 6 shows that if we compare the zero-points in counts s^{-1} to the effective gain we see a strong correlation between zero-point variation and effective gain variation in 2016A. In the 2017A and 2017B semester, the effective gain variation is much smaller and is not correlated with a zero-point change.

3.3. Image Zero-points versus MJD

We also examined the zero-point variation over time to see if there was any sign of accumulation of contaminants (*dust*) on the Mayall optical surfaces. Burke et al. (2018; their Figure 9) found a linear decrease in sensitivity for the CTIO Blanco and DECam during the DES; periodic washings restored the sensitivity. However, when we compared to the Mayall CO₂ cleaning schedule, Figure 7, we did not find a clear correlation with the cleaning schedule.

We do, however, note differences across seasons. Figure 8 shows a clear relationship between zero-point and PWV_{los} with

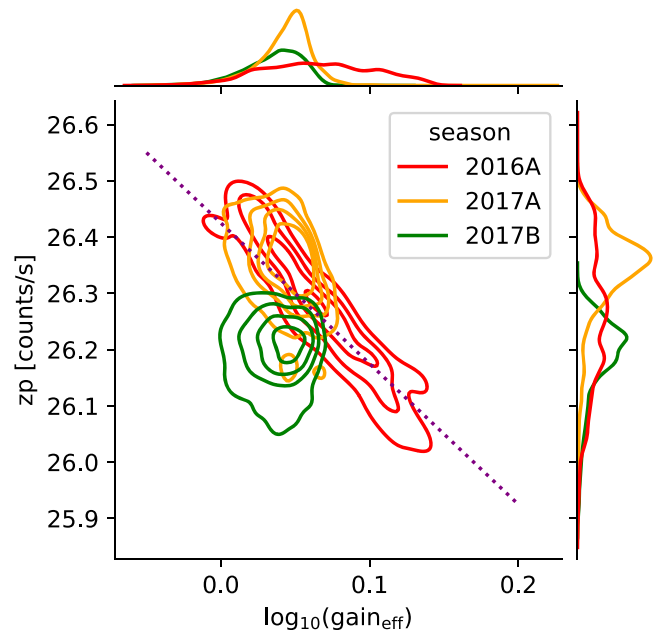


Figure 6. The zero-point (counts s^{-1}) vs. $\log_{10} g_{\text{eff}}$ visualized with a 2D kernel density estimate (solid lines) and projected distributions. Dotted line: an overlay of a -2.5 slope explains the variation of zp with $\log_{10} g_{\text{eff}}$ in 2016A, but not in the other seasons.

a constant offset between seasons. We normalize the zero-point so that the mode in each season is $zp = 26.5$ mag by adding the following: $(-0.0121, 0.0493, 0.1818)$ mag in seasons (2016A, 2017A, 2017B). Given the sparsity of data in 2016B, we ignore 2016B here and for the rest of this analysis. Including these per-season offsets reduced the NMAD of the zero-point to 61 mmag.

After accounting for this per-season variation, the remaining correlation between zero-point and MJD was marginal. Fitting

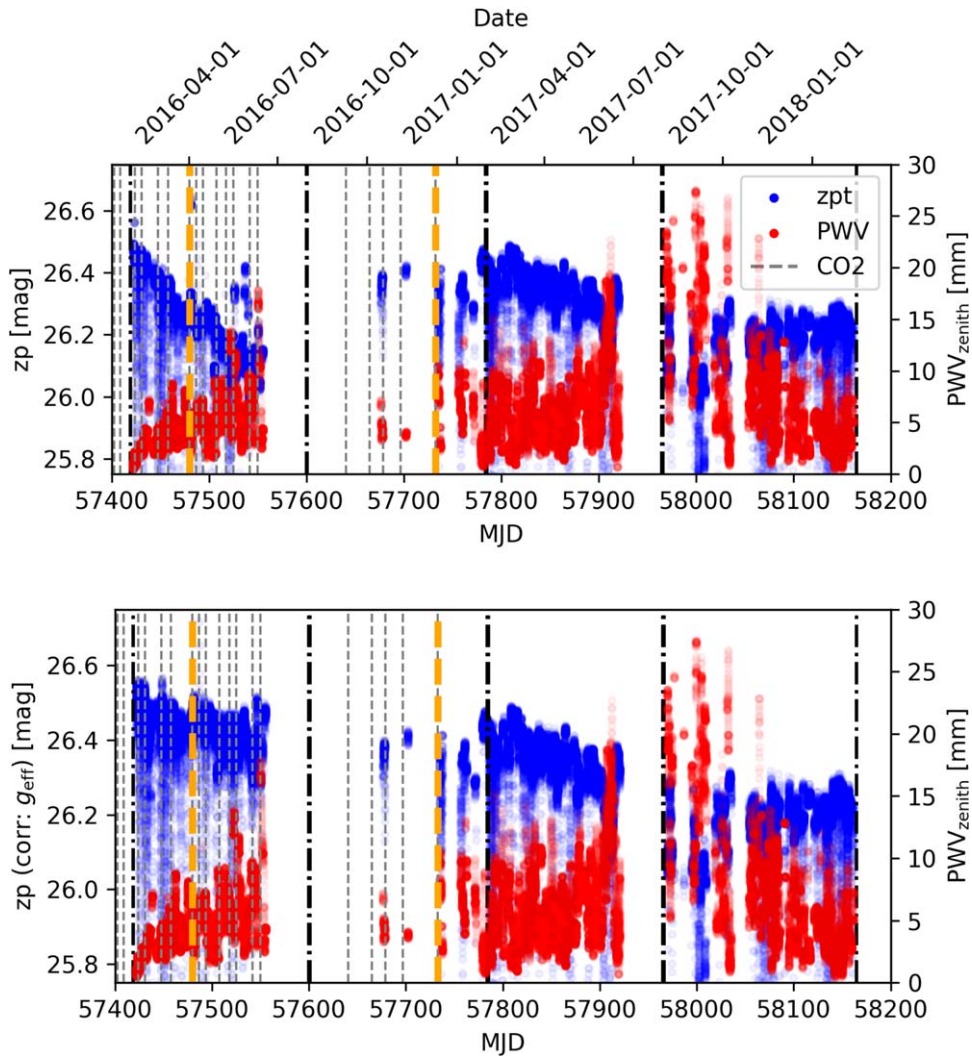


Figure 7. Top: MzLS image zero-points in counts s^{-1} (blue) along with the GPS-measured amount of PWV (red). There is a clear anticorrelation between the zero-point and PWV. But we also see an apparent secular evolution in time of the MzLS image zero-points in counts s^{-1} . This is due to the g_{eff} variation in 2016A. Bottom: the MzLS image zero-points in $e^{-} s^{-1}$ (blue) using the correction for 2016A discussed in Section 3.2. The anticorrelation with PWV is even more evident. Note the very clear decreases in sensitivity associated with the very high PWV levels at MJD $\sim 57,910$ and $57,980$ – $58,020$. Additionally, there is a clear per-season offset in the sensitivity. The cleanings of the Mayall optics (CO₂, gray dashed) and mirror washes (gold, dashed-dotted) are not clearly associated with any clear change in zero-point sensitivity.

for a simple linear MJD model across all seasons found a slope of < 0.01 mmag day $^{-1}$ that reduced the NMAD by < 1 mmag. Due to this low significance, we thus choose not to include such a physically somewhat motivated (dust accumulation), but essentially still ad-hoc model in this analysis.

3.4. Image Zero-points versus PWV

After correcting for the variation in the effective gain, a significant portion (23 mmag) of the remaining variation in the zero-points is well explained by the variation in PWV (Figures 7 and 8.) There are other sources of zero-point variation, most notably gray opacity from condensed water (clouds and ice), along with Mie scattering from aerosols and Rayleigh scattering from gas molecules. In the z band, the wavelength-dependent absorption from aerosols and Rayleigh scattering is almost flat and indistinguishable from a general gray opacity.

The GPS-based PWV measurement reports the PWV at zenith, PWV_{zenith} , based on the combination of measurements

of delays from several satellites spread across the sky with local meteorological data (pressure, temperature, humidity). Any given observation with the Mayall at an angle away from zenith will look through more water vapor. If we assume that the PWV is distributed as a uniform slab in the atmosphere,⁸ then the amount of water vapor along a given line of sight, PWV_{los} , will scale with the airmass, $X = \sec(\text{zenith angle})$,

$$PWV_{\text{los}} = PWV_{\text{zenith}} X. \quad (5)$$

However, the absorption does not scale linearly with the amount of water vapor. Water vapor absorption is a rich mix of lines, many of them at relatively high optical depth even at just a few mm of PWV. Thus the water vapor absorption displays a nonlinear relationship between total absorption in a given wavelength window and PWV column depth (see Figure 3).

⁸ The slab assumption ignores spatial correlations in PWV across different lines of sight through the atmosphere; however these effects are expected to be < 1 mm. This is supported by the results of Li et al. (2017) who found PWV changed by less than 1.0 mm in 90% of APOGEE spectra taken up to 70 deg apart within 1.5 hr.

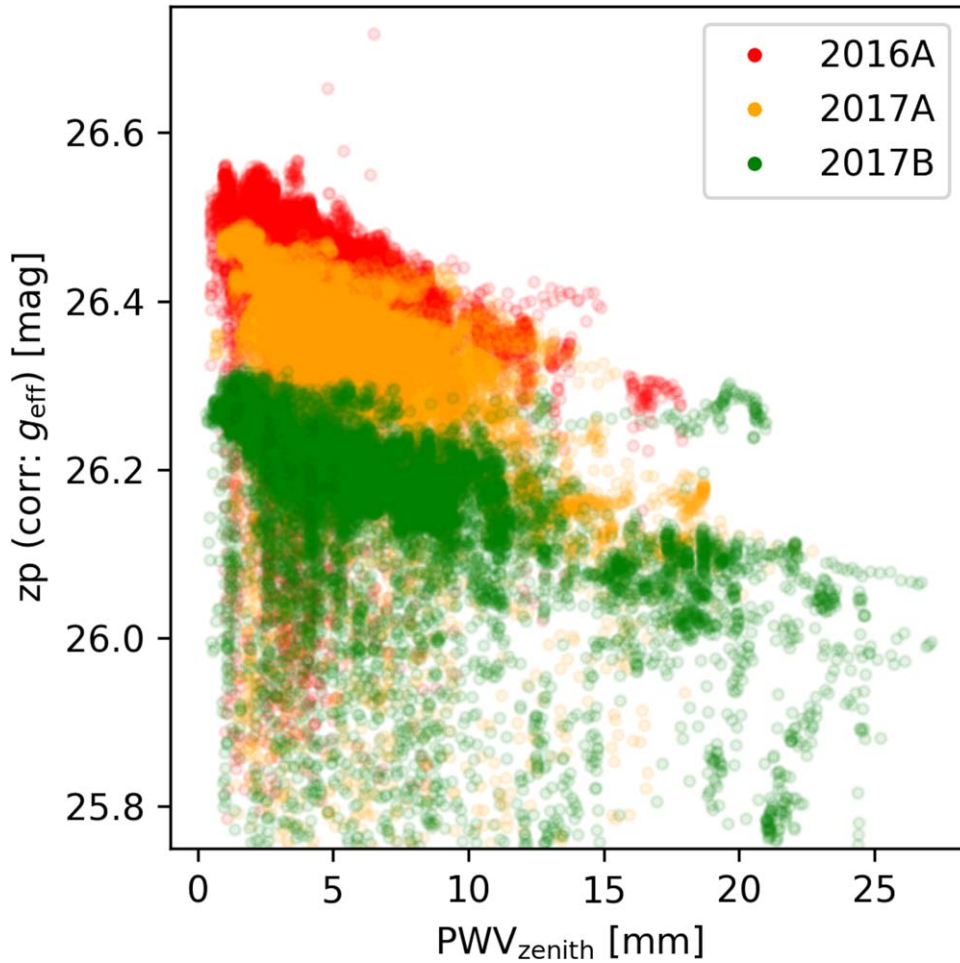


Figure 8. The zero-point sensitivity for the 54,985 “clean” z-band exposures in the MzLS survey. The color coding gives the MJD: red is 2016A, green is 2017A, yellow is 2017B. These zero-points are in $e^{-1} s^{-1}$ and are *not* corrected for the (zp, g_{eff}) correlation visible in Figure 6. The correlation between zero-point and PWV is evident, along with a per-season offset.

Table 2
Zero-point, PWV coefficients, NMAD

Zero-point Unit	PWV Type	Offset (2016A, 2017A, 2017B) (mmag)	PWV Slope ^a (mmag mm ⁻¹)	Mode mag	Median mag	NMAD (mmag)
counts s ⁻¹	26.3565	26.2681	129.9
e ⁻ /s	26.3825	26.3497	129.9
e ⁻ /s	...	(12.1, -50.4, -181.8)	...	26.4095	26.4013	59.6
e ⁻ /s	PWV _{Wade}		12.1	26.4815	26.4743	40.0
e ⁻ /s	PWV _{los} ^{eff}		31.8	26.5445	26.5281	38.1
e ⁻ /s	PWV _{los}		[17, 11]	26.5175	26.5017	38.8
e ⁻ /s	K9 star absorp		1	26.5385	26.5207	37.7

Note.

^a The units for the G2, K9 model absorption PWV slopes are 1 = mmag/mmag as the mm of PWV have already been translated through the K9 model to mmag of absorption.

Once an individual line saturates, the increasing water vapor column depth no longer leads to additional absorption, so the absorption increases with increasing PWV more slowly than linearly. While solving for PWV using forward models takes these effects into account, faster methods of spectral PWV extraction that simply map the line core intensity to PWV are sensitive to this effect (Thomas-Osip et al. 2007; Brault et al. 1975). Wade & Horne (1988) estimated that one could account for this saturation by calculating an effective line-of-sight PWV

by scaling by airmass to the $\delta = 0.6$ power:

$$\text{PWV}_{\text{Wade}} = \text{PWV}_{\text{zenith}} X^{0.6}. \quad (6)$$

This correction allows for a single linear coefficient to describe the increase in absorption (decrease in zero-point, zp) with airmass:

$$\text{zp} = \text{zp}_{\text{ideal}} - \beta \text{PWV}_{\text{zenith}} X^{\delta}. \quad (7)$$

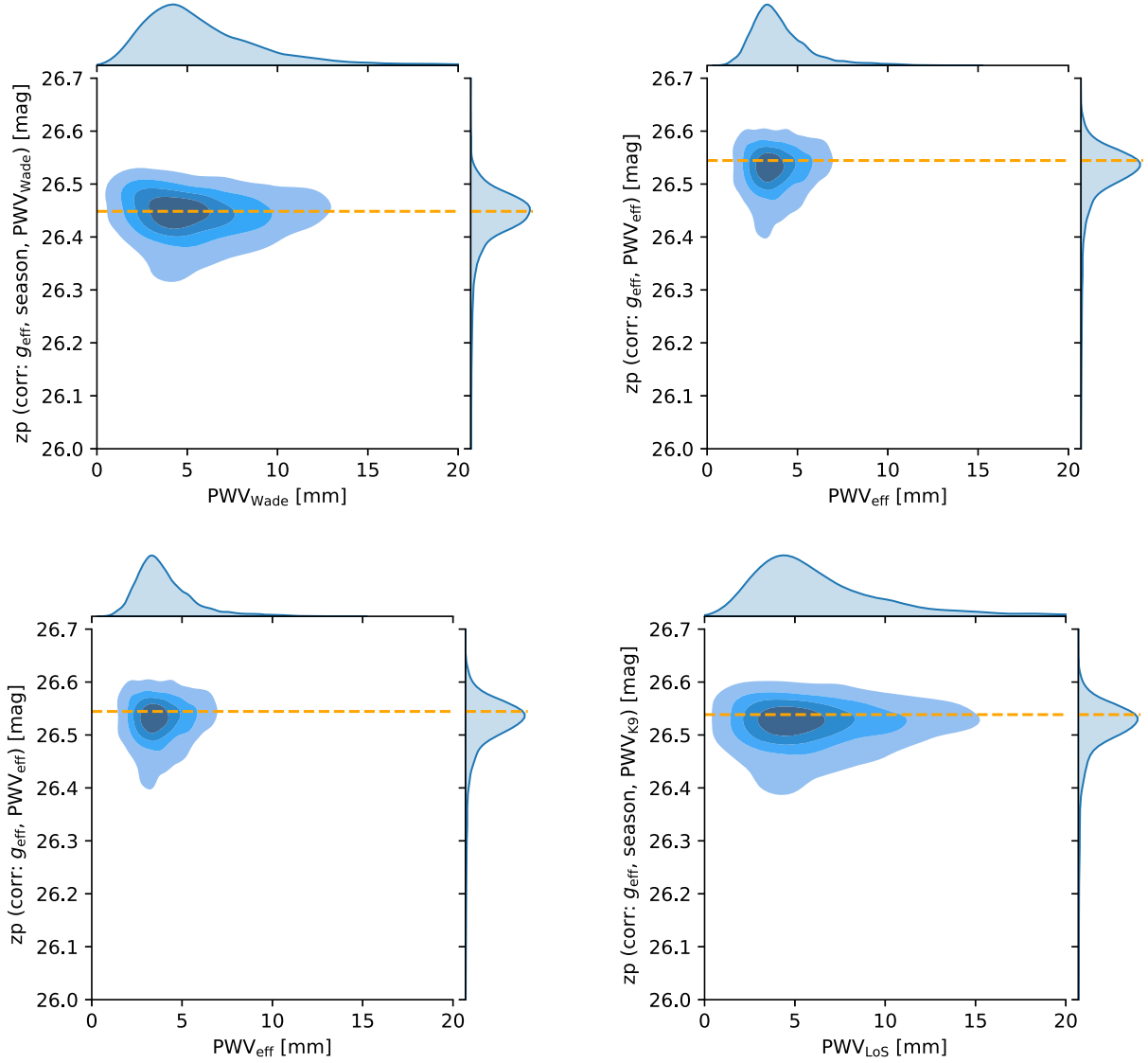


Figure 9. MzLS zero-point with PWV contribution removed for four different methods of calculating effective PWV absorption in z : (top left) corrected by $0.0121 \times \text{PWV}_{\text{zenith}}(X)^{0.6}$, $\sigma = 40.9$ mmag; (top right) $0.0318 \times (\text{PWV}_{\text{zenith}}X)^{0.6}$, $\sigma = 38.3$ mmag; (bottom left) same but plotted against PWV_{los} , $\sigma = 38.8$ mmag; (bottom right) corrected by the absorption expected for a K9 stellar model, $\sigma = 37.9$ mmag. The σ values are the NMAD for the distributions of adjusted zero-points (see Table 2). The shaded contour regions enclose (20%, 40%, 60%, 80%) of the points. The orange dashed horizontal lines are the mode of each zero-point distribution.

We find that for an assumed $\delta = 0.6$, a coefficient of $\beta = 12.1$ mmag mm $^{-1}$ provides an improved fit for translating the measured zero-points to an idealized constant zero-point.

While Wade & Horne (1988) gave the scaling as just in airmass $X^{0.6}$, physically the saturation effect should follow total water vapor along the line of sight, PWV_{los} ; i.e., looking through 10 mm of water vapor should yield the same absorption profile whether that is at $\text{PWV} = 10$ mm at an airmass of 1 or $\text{PWV} = 5$ mm at an airmass of 2. We set the normalization $\text{PWV}_{\text{norm}} = 2$ mm at the lowest value of PWV regularly measured in the data and model the zero-point as

$$zp = zp_{\text{ideal}} - \beta \left(\frac{\text{PWV}_{\text{zenith}} X}{\text{PWV}_{\text{norm}}} \right)^{\delta}. \quad (8)$$

For this definition of effective PWV, we find $\delta = 0.6$ makes the zero-point dependence largely linear with $\beta = 31.8$ mmag mm $^{-0.6}$. This corrected-effective-PWV prescription

explains the zero-point variation marginally better than the Wade prescription (see Table 2).

Using detailed water absorption and stellar spectral models, we can directly calculate the expected absorption of a given SED due to a given amount of water vapor along the line of sight. Any observation contains stars of many different stellar types, and the calibration will represent an aggregation across the range of stars. The full details of the calibration process depend on the choice of signal-to-noise weighting and the brightness-color distribution of objects, but we here illustrate the effect by using a single representative stellar type. For the MzLS data, we find that K9 star can represent the typical calibration and variation. If we are calibrating the zero-point using a K9-type star, then

$$zp = zp_{\text{ideal}} - \gamma \text{K9}_{\text{absorption}}(\text{PWV}_{\text{los}}), \quad (9)$$

where $\text{K9}_{\text{absorption}}(\text{PWV}_{\text{los}})$ is the predicted absorption of a K9 spectrum through PWV_{los} as integrated over the relevant

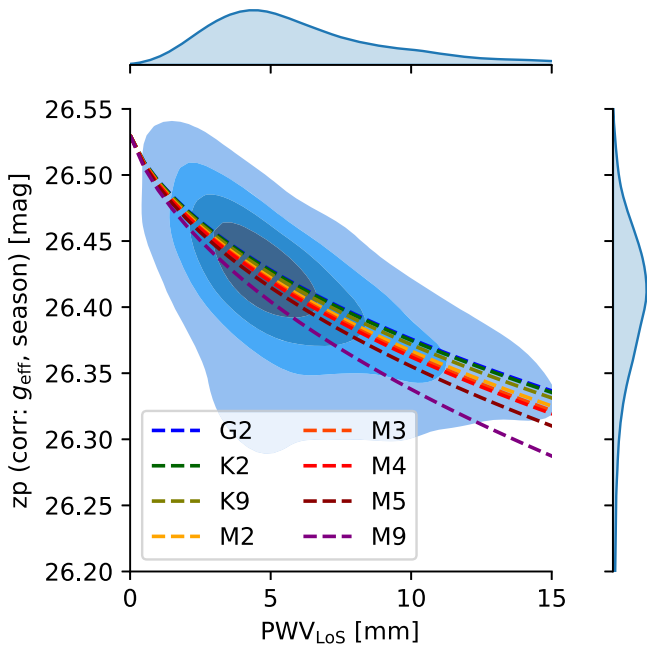


Figure 10. MzLS zero-point vs. PWV_{Los} . Overlaid in dashed lines are the expected change in z -band transmission when observing different stellar types: G2 (blue), K2 (dark green), K9 (olive), M2 (orange), M3 (orange-red), M4 (red), M5 (dark red), and M9 (purple). The shaded contour regions enclose (20%, 40%, 60%, 80%) of the points.

passband for which z_p is being determined. If we are correctly modeling all of the relevant physics, γ should be equal to 1.

If we use this prediction for a K9 star to model the zero-point variation for the MzLS data and fit for γ in Equation (9), we find $\gamma = 0.983 \pm 0.008$. While this linear fit value is formally well constrained, a value of $\gamma = 1$ yields the same NMAD of the residuals of 37.9 mmag. We thus fix $\gamma = 1$ for the stellar +PWV model term. Figure 9 compares the distribution of the residuals after fitting with each of Equations (7), (8), and (9) (with $\gamma = 1$).

Figure 10 shows the expected zero-point offsets as a function of PWV for different stellar types overlaid with the MzLS zero-points. The calculation of these offsets is described in detail in Section 5.1.

Table 2 summarizes the coefficients for the different models for zero-point based on PWV. Accounting for the variation in PWV reduces the NMAD of zero-point residuals from 61 mmag to ~ 40 mmag, depending on the exact treatment of PWV. Because these terms add in quadrature, that implies that PWV leads to 45 mmag of gray variation in the zero-point. We attribute the majority of the remaining 40 mmag of zero-point variation to the following (in increasing order of contribution): (1) CCD temperature variation; (2) uncertainties in the reference catalog; (3) calibration variations in the MzLS processing pipeline; and (4) other atmospheric sources. We summarize these contributions in Table 3.

- (1) CCD temperature variation can change the long-wavelength response of CCD detectors due to phonon+photon excitation. However we find that these effects are not significant at the $\lambda < 1000$ nm regime of these thick CCDs and estimate an upper limit of < 5 mmag for the contribution of CCD temperature variation to sensitivity variation. See Appendix for more details.

Table 3
Estimated Contributions to Zero-Point Variation

Source	Contribution (mmag)
PWV	45
Atmospheric gray opacity: clouds, ice, Rayleigh, Mie scattering	37
Processing pipeline: aperture corrections, effective gain	16
Reference catalog	10
CCD temperature	< 5
Total	61

Note.

^a The CCD temperature was constant within 2 degrees C for the duration of the survey. While even this level of variation might lead to a sensitivity change, we find no evidence of any detectable correlation of zero-point variation with CCD temperature. See Appendix for more details.

- (2) The reference catalog is the PS1 catalog, with a quoted uncertainty of ~ 10 mmag (Schlafly et al. 2012). While any errors in the reference catalog would be constant for a given region of sky, they would appear as variations in the calculated zero-point when comparing observations across the sky. We thus estimate that errors in the reference catalog contribute ~ 10 mmag of the zero-point variation.
- (3) The details of calibration steps in the MzLS processing pipeline details, such as infinite-aperture corrections and per-amp normalization, can affect the $e^- s^{-1}$ zero-point, even while resulting in totally fine magnitudes in the final catalog. We estimate that the dominant uncertainties are likely from our estimation of the effective gain from looking at sky noise. We find an intra-night variation in our effective gain correction in 2016A equivalent to 16 mmag of the predicted zero-point variation.
- (4) Atmospheric sources other than PWV include the gray absorption from clouds and ice along with smoothly varying absorption from atoms and simple molecules (Rayleigh) and aerosols (larger molecules, Mie). We attribute the remaining observed variation of 37 mmag to these other atmospheric sources.

A first-glance estimation might lead one to conclude that not being able to resolve PWV variation better than 1–2 mm would lead to a potential ~ 15 –30 mmag irreducible variation (for z_p/PWV slopes of 0.017–0.011 mmag mm^{-1} from the PWV_{Los} model). But that is not the relevant calculation here. The fact that the zero-point variation is strongly correlated with PWV means that there is in fact significant power in a gray approximation of PWV—this gray offset is what the zero-point variation is already capturing. In other words, if PWV were gray in its effect on opacity or if all objects had the same SED, the catalog zero-points would be correct. The key part of properly accounting for PWV is the *differential* effect of the PWV-absorption spectrum within the passband. We explore this differential aspect, which varies by SED of the source, in more detail in Section 3.5, 4, and 5. As a brief preview, we find that the differential effect to be ~ 2 mmag mm^{-1} .

We provide detailed fits for zero-point sensitivity as a function of PWV for different estimates of PWV in Table 4.

Table 4
Per-season PWV Slope and Offsets, NMAD

PWV type	Season	Offset (mmag)	Offset Err (mmag)	PWV Slope ^a (mmag mm ⁻¹)	PWV Slope Err ^a (mmag mm ⁻¹)	Mode mag	Median mag	NMAD (mmag)
PWV _{Wade}	2016A	-34.5	1.4	11.1	0.27	26.5305	26.5223	39.1
	2017A	-85.0	1.2	14.7	0.18	26.5335	26.5183	41.0
	2017B	-259.3	1.2	8.4	0.11	26.5235	26.5198	34.1
PWV _{los} ^{eff}	2016A	+0.8	2.3	26.6	0.65	26.5355	26.5224	39.1
	2017A	-30.6	2.0	34.9	0.46	26.5305	26.5196	40.8
	2017B	-210.8	1.8	23.8	0.32	26.5245	26.5205	30.1
PWV _{los}	2016A	-35.3	1.4	10.7	0.26	26.5345	26.5224	39.0
	2017A	-89.4	1.2	13.0	0.15	26.5345	26.5184	39.7
	2017B	-260.6	1.2	6.8	0.09	26.5185	26.5198	32.7
K9 star absorp	2016A	-2.4	2.2	0.86	0.021	26.5385	26.5225	39.1
	2017A	-30.3	2.0	1.17	0.016	26.5325	26.5202	40.9
	2017B	-204.8	1.8	0.85	0.011	26.5215	26.5208	30.0
...	2016A	-87.7	0.7	0	...	26.5295	26.5198	56.0
	2017A	-168.3	0.7			26.5235	26.5209	59.4
	2017B	-330.6	0.8			26.5545	26.5262	60.7
PWV _{Wade}	2016A	-29.6	0.6	12.1	...	26.5375	26.5226	38.5
	2017A	-94.5	0.6			26.5385	26.5185	41.6
	2017B	-227.7	0.7			26.5095	26.5129	35.0
PWV _{los} ^{eff}	2016A	+18.2	0.6	31.8	...	26.5385	26.5230	37.4
	2017A	-43.1	0.6			26.5335	26.5200	40.6
	2017B	-170.6	0.7			26.5095	26.5163	35.1
PWV _{los}	2016A	-9.3	0.6	[17, 11]	...	26.5405	26.5232	37.1
	2017A	-69.0	0.6			26.5365	26.5193	40.0
	2017B	-189.6	0.8			26.5025	26.5103	39.8
K9 star absorp	2016A	+12.1	0.6	1	...	26.5385	26.5228	39.1
	2017A	-50.4	0.6			26.5385	26.5207	40.3
	2017B	-181.8	0.7			26.5195	26.5186	32.9

Note.

^a The units for the K9 model absorption PWV slopes are 1 = mmag/mmag as the mm of PWV have already been translated through the K9 model to mmag of absorption.

3.5. MzLS Per-exposure Magnitude Deviations Depend on Color and PWV

The DESI Legacy Survey DR9 provides per-image forced photometry. We here explore the correlation between the per-image measured magnitude of a star, its color, and PWV.

First, we offer some definitions for what will be a confusing discussion of differences of differences. If z_j^i is the z -band magnitude for star i measured on image j , then we are interested in $\Delta z_j^i = z_j^i - \langle z^i \rangle$, where $\langle z^i \rangle$ is the average⁹ magnitude based on all of the survey images. $\text{PWV}_{\text{los } j}$ is the measured PWV_{los} for image j .

The stars observed by MzLS span the range of stellar types from F5–M4 stars (Figure 11). We here look at the relative change in z -band flux of specific objects under varying amounts of PWV as a function of object color. We group stars into three broad color categories: “blue,” $r - z \leq 0.5$ mag; “green,” $0.5 \text{ mag} < r - z \leq 1.2$ mag; “red,” $1.2 \text{ mag} < r - z$. While these color ranges are only loosely motivated, they end up being illustrative. The “blue” cut is in the middle of G-type stars—the mean color of the PS1 stars used to establish the MzLS calibration is close to a K9 (see Figure 20). The “red” cut marks the beginning of the M-dwarf sequence, which is where the stellar locus goes vertical in $r - z$ versus $g - r$. The g - and r -

band magnitudes are from the Bok 90 observations from the Beijing-Arizona Sky Survey (BASS)¹⁰ component of the DESI Legacy Survey, and the z -band magnitudes are determined from the MzLS observations.

Figure 11 shows a (median, mean) $r - z$ color for MzLS observed stars of (0.85, 0.97) mag. A K9 dwarf star has a color of $r - z = 0.93$ mag, which is right in between these values. Thus even without fully recreating the calibration of the MzLS survey, one would still reasonably expect that this typical color will remain correctly calibrated through a variety of PWV conditions. These blue–green and blue–red relations should cross through zero when the conditions match the “average” conditions of the set of data considered by the MzLS catalog calibration. At higher PWV_{los} , the progressively bluer (redder) stars should be brighter (fainter).

The DESI Legacy Survey is divided into $0^\circ.25 \times 0^\circ.25$ “bricks” on the sky. We restrict our analysis to stars in bricks that had a median of three or more exposures contributing to the pixels in the brick: “nexp_z > 3.” This reduced our sample from 93,610 bricks to 81,934 bricks. We successfully retrieved photometry for 81,1156 of these bricks, which had data from 15,381 MzLS exposures. The Mosaic3 field of view is $36' \times 36'$, which means that 36 bricks fit exactly into one field of view. The alignment is not perfect, in part by construction, and so 60 bricks should be relevant for any particular image.

⁹ It is not strictly an average. See Legacy Survey paper for details.

¹⁰ <http://www.legacysurvey.org/bass/>

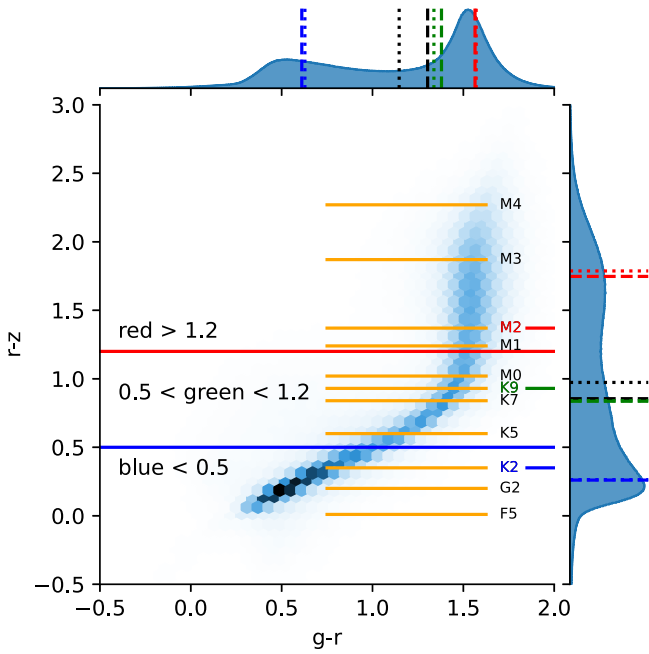


Figure 11. Stellar locus for DESI Legacy Survey stars in the MzLS footprint. No correction has been made for Milky Way extinction. The blue, green, and red $r - z$ color regions are indicated along with the nominal $r - z$ colors of a range of stellar types. The top (side) panels are the projected histograms for $g - r$ ($r - z$). The overall median (black dashed) and mean (black dotted) colors are consistent with a K9 star. For each color region, the median (colored dashed) and mean (colored dotted) value are very close. Representative stellar types of K2, K9, and M2 are denoted in (blue, green, red). Note that, while the nominal mean/median red color is notably redder than the M2 (M2.0) stellar spectrum, it is still within the range between M2 and M3.

We restrict our stellar sample to objects identified as stars and with z -band signal-to-noise ratio (S/N) > 25 , $0.5 \text{ mag} < g - r < 2.5 \text{ mag}$, and $0.5 \text{ mag} < r - z < 5.0 \text{ mag}$.

Figure 12 shows how the variance in Δz is a function of magnitude. Nonlinearity/saturation drives up the variance at the brighter end while decreasing S/N , and increasing the nonstellar contamination drives up the variance at the faint end. We thus further restrict our Δz versus PWV analysis to stars in the range of $17 < z < 20 \text{ mag}$.

For each image, and each color class, we compute the median of the distribution of Δz_j^i values. Each image, j , then has three values: Δz_j^{blue} , $\Delta z_j^{\text{green}}$, Δz_j^{red} .

Figure 13 shows the trends of $\Delta z_j^{\text{blue,green,red}}$ versus $\text{PWV}_{\text{los } j}$. As PWV_{los} increases, Δz_j^{blue} becomes brighter, $\Delta z_j^{\text{green}}$ is flat, and Δz_j^{red} becomes fainter. This trend as a function of stellar type is consistent with a model where SEDs that are bluer or redder than the average are miscalibrated, because an effectively gray term (the zero-point in the natural system) does not properly capture the significant absorption due to PWV at the red side of the z band. If the absorption were at the blue side of the z band, then the slopes would be reversed, with the blue stars being fainter at higher PWV and the red stars being brighter—relative to the green stars. The flat trend in the green stars implies that they are representative of the effective average star used to calibrate the MzLS observations.

They are thus flat in Δz versus PWV_{los} . For PWV_{los} less than this value, the red stars are systematically brighter than their average. For PWV_{los} greater than this value, the blue (red) stars are systematically brighter (fainter) than their average. The

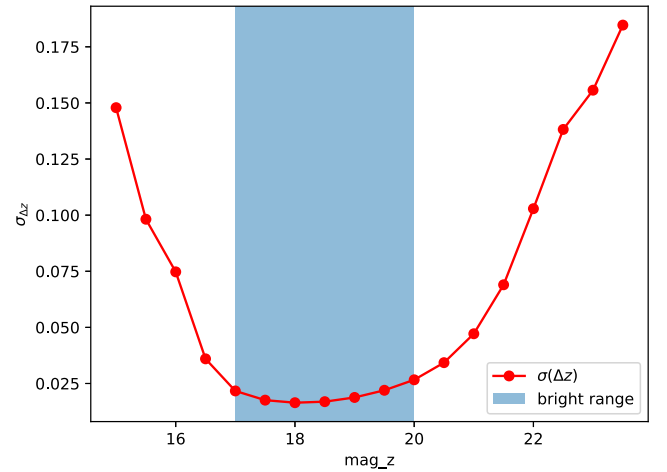


Figure 12. Standard deviation of Δz for all stars in MzLS. Red points+line: $\sigma(\Delta z)$ binned by magnitude. At bright magnitudes, the variance increases as measurements approach the saturated/nonlinear region. At the faint end, the variance increases as S/N decreases. Blue rectangle: magnitude range of the “bright” sample that we focus on in our Δz vs. PWV analysis.

three binned lines meet at $\Delta z = 0 \text{ mag}$ at the median PWV_{los} of the survey, $\sim 4.83 \text{ mm}$.

Comparing the relative trend makes the correlation clearer. Figure 14 clearly shows that there is a dependence of $\Delta z_j^{\text{blue}} - \Delta z_j^{\text{green,red}}$ with PWV across the full range of measured PWV values. The dependence is well explained by the detailed PWV absorption against the stellar templates from Section 5.1, but also by a simple linear fit to PWV_{los} with a dependency of $-0.299 \text{ mmag mm}^{-1}$ for blue–red, and $-0.114 \text{ mmag mm}^{-1}$ for blue–green. Figure 22 in Appendix B of Burke et al. (2018) compares two different DECam exposures, one at a low $\text{PWV}_{\text{zenith}}$ and one at a high $\text{PWV}_{\text{zenith}}$. They find a clear difference in the dependence of Δz across 14 bins of stellar $g - i$ color. Our Figure 13 only divides the sample into three color bins but shows 32 bins of PWV_{los} .

Note that $\Delta z_j^{\text{blue,green,red}}$ being 0 at the median PWV_{los} of the survey is not dependent on the relative calibration of the blue, green, and red stars in the reference catalog. We are here looking at the *difference* between the per-epoch magnitude and the overall average survey magnitude of the star. We clearly detect the slope due to PWV_{los} and show that it is explained by variation in the differential PWV absorption of stellar spectral types matching the stellar colors.

Figure 15 shows the dependence of Δz (blue – red) = (median blue Δz) – (median red Δz) versus MJD. Because there is little correlation between MJD and PWV on these scales, the distribution should not be expected to show any clear trends. The deviations are still there; they have just been scrambled up by looking at MJD instead of PWV_{los} . The notable exception is the deviation between MJD 57,950–58,010. This time at the beginning of the 2017A season was a particularly high PWV period with $\text{PWV}_{\text{zenith}} > 15 \text{ mm}$ (see Figure 7). The Δz (blue – red) variation provides an independent indication that the zero-point variation had a strong color term during these nights.

We thus have a consistent picture. Our PWV model explains the zero-point variation from the MzLS survey assuming the images were calibrated against a set of stars with a median color of a K9 star. The color-based residuals for stars of different stellar types are then further consistent with the difference between the effect of PWV on K9 stars and those different types. Specifically, the red stars have a median

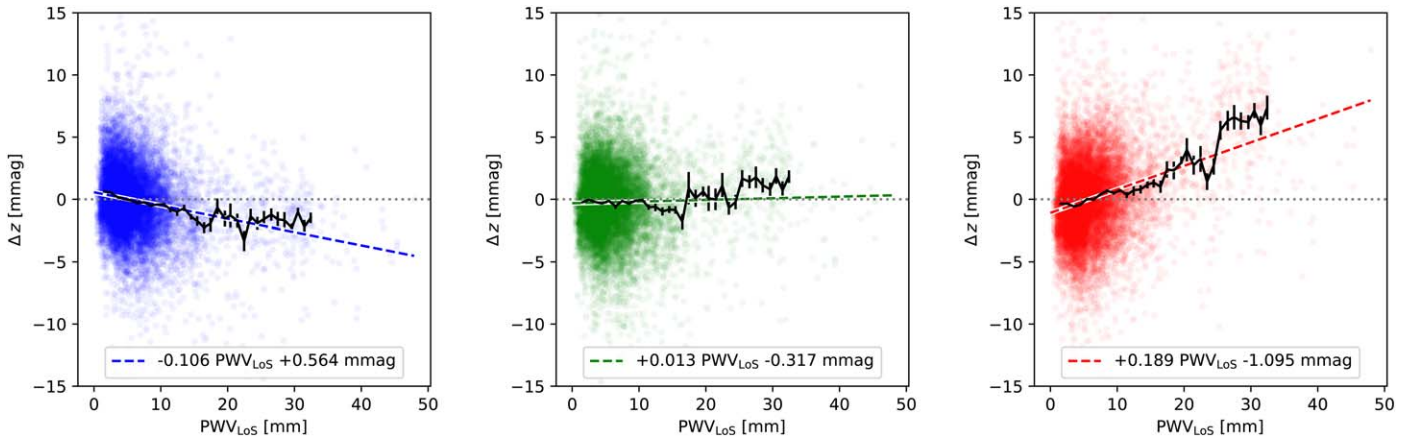


Figure 13. The per-observation variation of the z -band magnitude of stars in three color bins vs. the PWV_{los} for that observation. Left (blue): $r - z < 0.5$ mag. Center (green): $0.5 < r - z < 1.2$ mag. Right (red): $r - z > 1.2$ mag. Each point is the median Δz for all of the stars in that color bin for that observation. The median star in MzLS has a $r - z$ a bit less than 1 mag, and so the “green” panel is largely flat. The blue stars appear brighter at higher values of PWV, while the red stars are clearly fainter for high values of PWV. These binned lines intersect at the median PWV_{los} of the survey: ~ 4.83 mm.

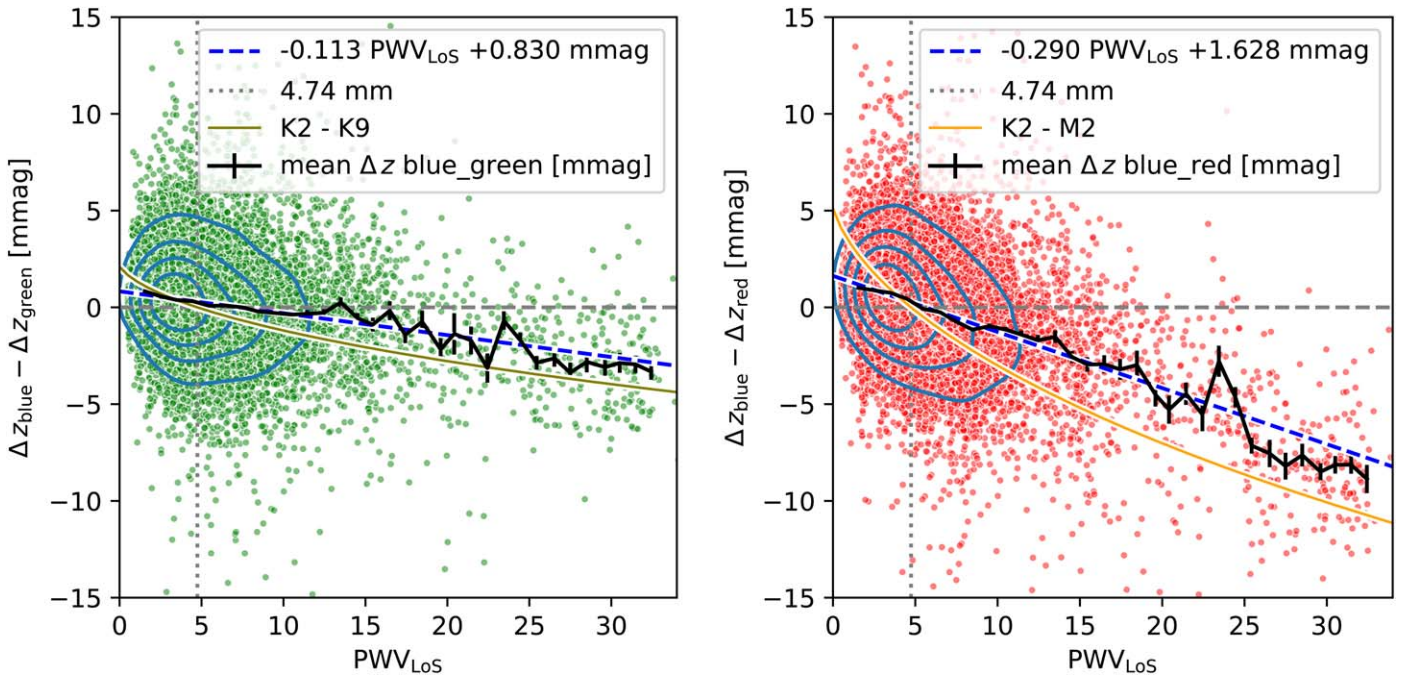


Figure 14. Difference in median Δz between different color stars vs. PWV_{los} (blue points, with density estimation contours as solid lines enclosing (20%, 40%, 60%, 80%) of the points). Left (blue–green): these are blue points minus the green points from Figure 13. Right (blue–red): these are blue points minus the red points from Figure 13. This correlation is reasonably explained by the variation of the calibrated brightness of a M4 star calibrated with a K9 star (orange solid line) through different PWV_{los} as shown in Figure 19. This model has been set to 0 at the median PWV_{los} value of 4.83 mm. The correlations for each color difference are reasonably explained by a simple linear fit (green dashed line), which reinforces the utility of using PWV_{los} as a practical quantity to understand the effect of PWV on absorption. Note that, because this is the $\Delta z_{\text{blue}} - \Delta z_{\text{red}}$, negative values here mean that the inferred magnitudes of red stars are fainter than those of blue stars compared to their average magnitudes. Thus negative values are consistent with increased absorption due to PWV. This is the same convention as in Figure 19.

magnitude offset with respect to the blue stars that is consistent with the difference in PWV absorption between M4 stellar spectra and K9 stellar spectra.

4. Correcting Zero-point with Δz (Color) versus PWV

Section 3.5 demonstrated that the variation in relative brightness of stars of different colors is correlated with PWV. We here explore whether the PWV data provide additional improvements in zero-point over just using the variation in relative brightness of the stars. The question is about the basic variation of each

measurement, the correlation with ero point, and the outliers. An additional important question is whether the color data can supplement cases where the PWV measurements have aberrations. One could of course ask the question the other way: “Can PWV help identify cases where the color-based, differential brightness of stars are incorrectly calibrated?” But it would be unclear what to then do about those data. If the color-based, differential brightness was systematically in error (rather than just noisy), that would imply that there was something wrong in the basic extraction of flux from the image.

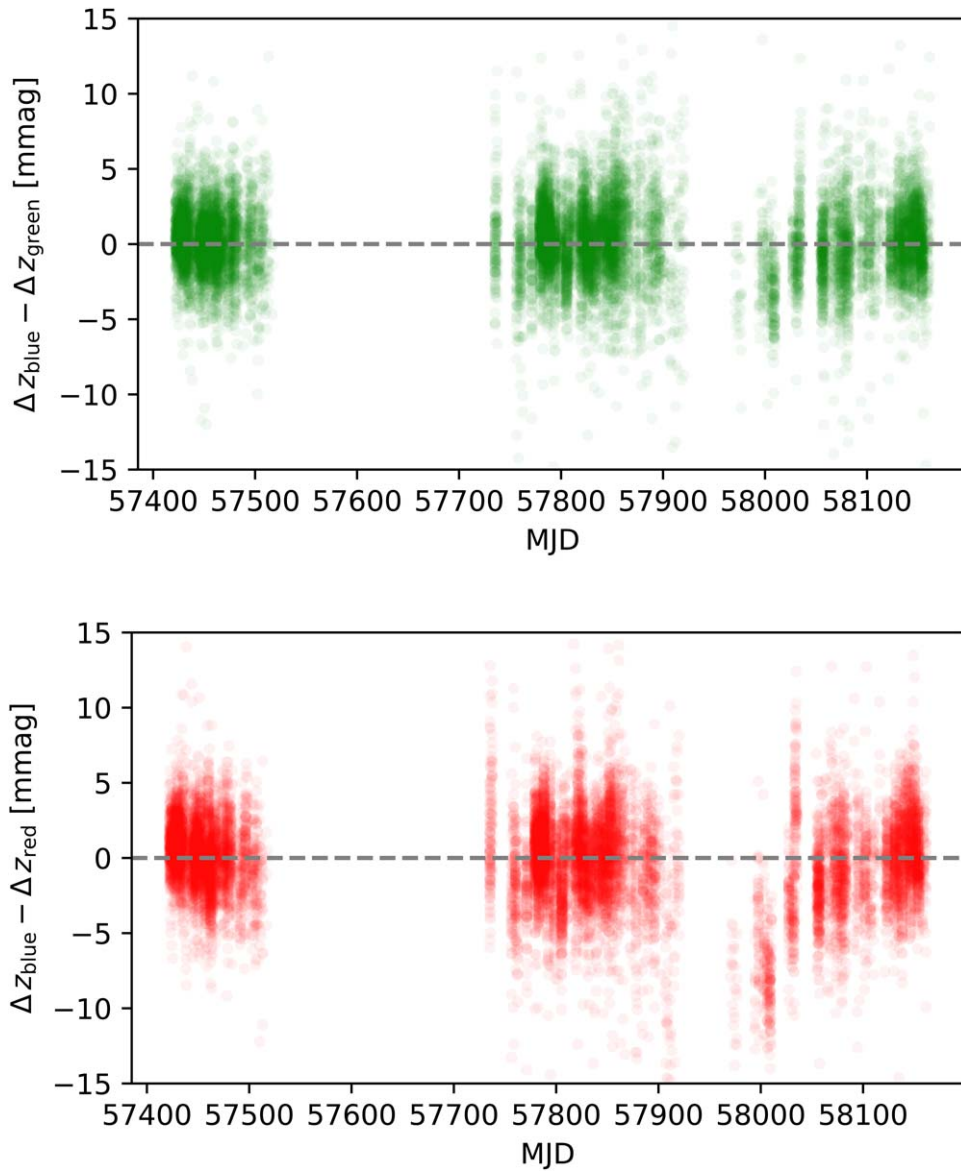


Figure 15. Left: the Δz (blue – red) vs. MJD. Right: the Δz (blue – red) vs. MJD. No correction has been made for PWV. The only clear trend is the deviation near MJD = 57,950–58,010, which is the time period with the highest PWV ($\text{PWV}_{\text{zenith}} > 15 \text{ mm}$) during the survey.

Figure 16 shows that Δz (blue – red) and PWV_{los} are clearly correlated, and the more negative values of Δz (blue – red) and higher values of PWV_{los} are both associated with less transparent conditions (lower zero-points). However, the PWV_{los} distributions (top panel) separate much more clearly with respect to the zero-point than do the Δz (blue – red) measurements (right panel).

Figure 17 demonstrates the success of using PWV_{los} to predict MJD-trend-corrected zero-point. The expected relationship across several stellar types explains both the core of the zero-point variation as well as the outliers. There are a noticeable number of outliers that have lower values of the zero-point even at low values of PWV_{los} . However, these images also have low Δz (blue – red) (refer back to Figure 16), and we hypothesize that these images have some amount of gray extinction. The residual of zero-point versus the predicted-stellar-model dependence on PWV_{los} does not appear to be obviously correlated with Δz (blue – red).

Figure 18 shows that Δz (blue – red) is indeed correlated with Δz (blue – red), but is not as powerful at predicting the zero-point variation, particularly at the highest level of PWV.

We conclude that PWV_{los} is a significantly better predictor of zero-point than Δz (blue – red). Measurements of PWV_{los} can improve the standard deviation of the measured zero-point from 58 mmag to 30 mmag. Using an admittedly simple, linear model of Δz (blue – red) to attempt to improve the zero-point variance results in a worse standard deviation of 69 mmag.

We end this section by mentioning two opportunities to improve the differential-brightness color-based measurement of PWV: (1) surveying with more repeated observations of fields in more filters; and (2) taking advantage of the temporal and spatial correlation of PWV.

MzLS was a survey conducted in a single band with a typical limit of only three repeated observations of a star. It is possible that results for color-dependent Δz could potentially be improved in surveys that have more repeated observations

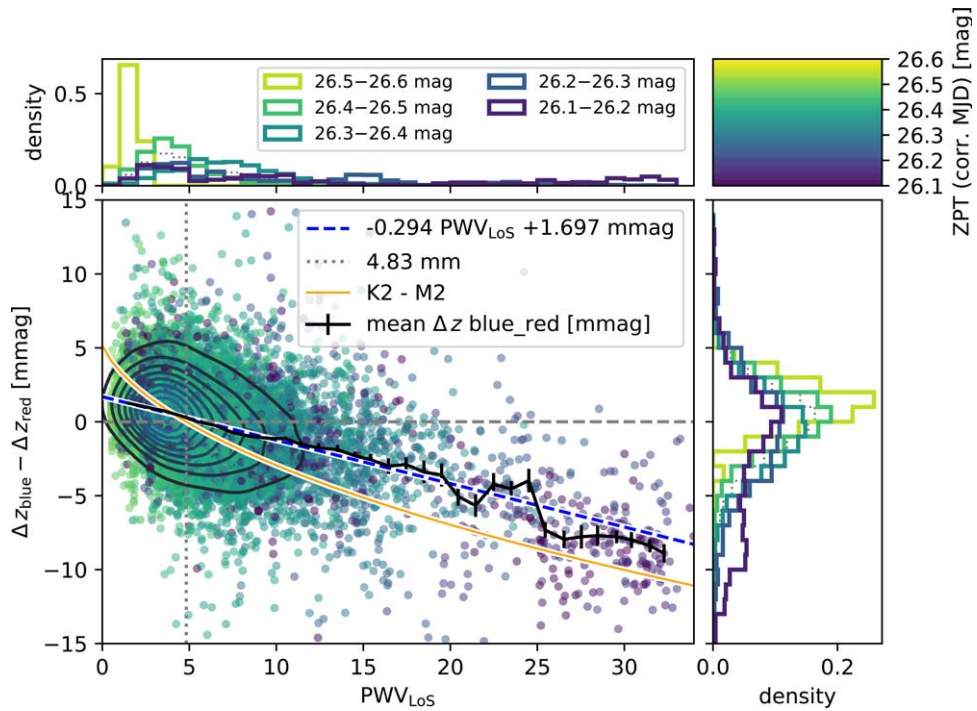


Figure 16. Δz (blue – red) vs. PWV_{los} , color-coded by zero-point. The trend in Δz (blue – red) vs. PWV_{los} is approximately linear in both the mean binned values (black line with errorbars) and a simple linear fit (blue dashed line). A model based on the expected difference in the relative brightness of a M2–K2 star qualitatively agrees with the trend (orange line). The top (side) panels give the projected distributions of PWV_{los} (Δz (blue – red)) for different values of the zero-point. The PWV_{los} measurements separate much more clearly than the Δz (blue – red) measurements. Note that the highest measured values of PWV_{los} consistently result in outlier zero-point measurements.

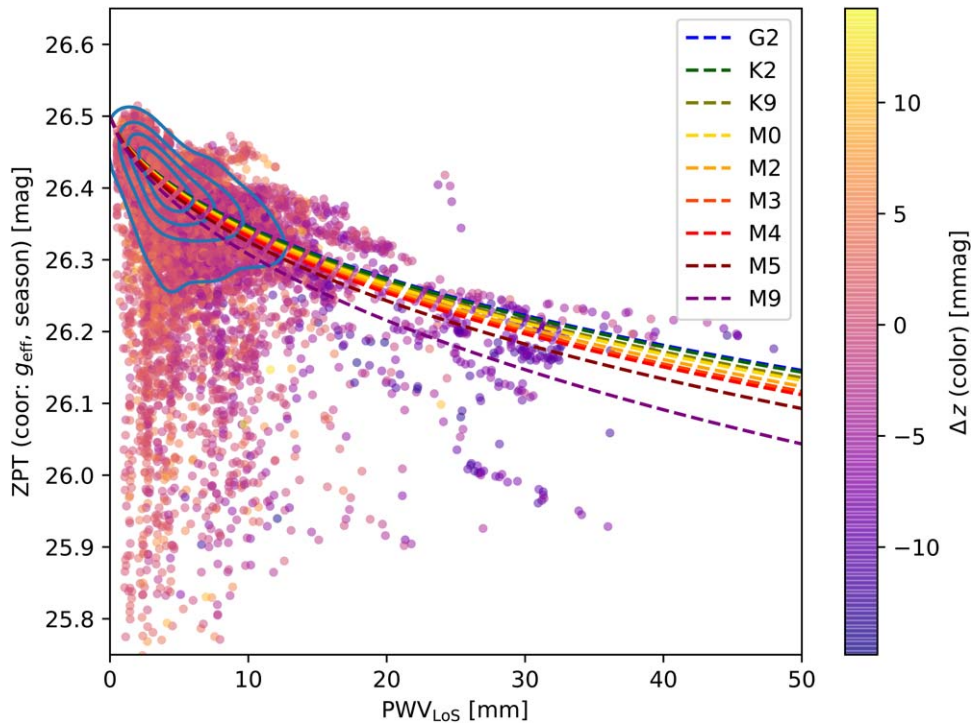


Figure 17. MzLS zero-point vs. PWV_{los} , and color-coded by Δz (blue – red). The contour lines enclose (20%, 40%, 60%, 80%) of the points. Overlaid are the predicted effect of PWV_{los} on six stellar templates: G2 (blue dashed line), K2 (forest-green dashed line), K9 (olive dashed line), M2 (orange dashed line), M4 (red dashed line), M9 (purple dashed line). The points with the largest PWV_{los} have clearly reduced z-band sensitivity and are also significantly negative in Δz (blue – red). While there is visible population of zero-point variation that is not explained by PWV, these also exhibit small excursions in Δz (color). We thus attribute these to gray extinction variation. Also note that while those outliers are very visible in the scatter plot, they are in fact a small fraction of the overall population, as indicated by the contour lines of the overall distribution.

over different conditions of the same field, or taking several images in different filters within an \sim hour to capture more directly the effects of PWV versus gray extinction. The gray extinction variation can be dominant over the effect of PWV. Thus measuring the gray extinction separately might allow for a cleaner differential-brightness color-based measurement of the effect of PWV.

The model of a uniform slab across the sky varying on 30–60 minute timescales is remarkably good, and the on-sky spatial variations of PWV are expected to be low (Li et al. 2017). Significant variations in PWV across the sky were generally only observed in the presence of atmospheric pressure fronts. The presence of such weather systems is generally anticorrelated with astronomical observing. Greater power may come from including in the model the strong temporal correlation of PWV as well as any small-amplitude spatial correlations on the sky. For example, it is possible that assuming some time constant for variation of PWV would allow the combination of measurements across a set of images to improve the sensitivity of using the differential-brightness color-based method to better predict the true telluric transmission spectrum.

5. Impact on Selected Science Cases

We have established that PWV explains the nonsecular zero-point variation of the MzLS survey and that there is a color-dependent effect for the inferred magnitudes of stars of different colors and spectral types. We next explore the consequences for PWV absorption for a wider variety of objects. We calculate the expected, induced photometric error for a variety of the object SEDs grouped into stars, supernovae, and quasars.

5.1. Stars

Achieving both accuracy and precision in ground-based stellar photometry requires a full understanding of the system transmission function, including the variable atmosphere. In particular, objects whose SEDs differ from the reference catalog stars are affected differently by variable PWV absorption. Color terms can handle smooth differences in SEDs, which is particularly effective when looking at the Rayleigh–Jeans tail of stars. However, cooler stars, particularly M, L, and T stars, (a) peak in emission at NIR wavelengths; and (b) have very nonblackbody SEDs with complex molecular-band features. The impact of second-order telluric absorption effects interferes with achieving precise photometry for exoplanet transit searches (e.g., Baker et al. 2017). Accurate colors are additionally important for reliable object classification.

To demonstrate the effect that PWV absorption has on stellar photometry, we integrate PHOENIX models (Husser et al. 2013) multiplied by a TAPAS water vapor transmission model scaled to different PWV values. These spectra are then integrated over filter profiles to compute the flux in each band as a function of PWV. These fluxes are converted to magnitudes in each band, m , referenced to a PWV of 0 mm such that $\Delta m = m(\text{PWV}) - m(\text{PWV} = 0)$. In Figure 19, we show Δm for the r , i , and z passbands in the top panels of each figure for K9, M4, and M9 spectral types.

In the MzLS catalog, the typical reference star used for calibration is a K9 dwarf (see Figure 20). A zero-point

estimated for these reference stars does not correctly include the effects of PWV absorption on the integrated photometry of redder stars. The bottom panels in Figure 19 show this expected zero-point error by plotting the difference in the effect of PWV absorption for K9, M4, and M9 stars. In nominal observing conditions (PWV = 5 mm), the error in the z -band calibrated brightness of M4 and M9 stars is 8 and 25 mmag, respectively, when calibrating with a K9 star. If instead an M4 star is used as a reference in calibration, an M9 star still has a significant brightness error of 17 mmag. This comparison shows how sensitive the effect is for stars with SEDs that vary quite substantially over a seemingly small temperature range. In the i band, the differential extinction between M4 and K9 stars is near zero whereas an M9 star would still experience a 5 mmag error. Due to the minimal amount of absorption in the r band, the error in this band is below 2 mmag for each star.

The $i-z$ color error due to these incorrect zero-point corrections for an M9 star are as follows: 15 mmag bluer at $\text{PWV}_{\text{los}} = 5$ mm and ~ 30 mmag bluer at $\text{PWV}_{\text{los}} = 10$ mm. Of importance to time series data is how the magnitudes would change in time as PWV_{los} changes between observations. For this, the slopes of the curves in Figure 19 show that the z -band magnitude for M4 and M9 stars referenced to a K9 star will change approximately 2 and 5 mmag per millimeter change in PWV, respectively, in drier conditions typical of conditions at KPNO (and Cerro Pachón).

5.2. Supernova Cosmology

The use of Type Ia supernovae (SNe Ia) as cosmological probes relies on them having homogeneous light curves with standardizable luminosities at the time of peak brightness. By calibrating for intrinsic variations between the absolute magnitudes of individual SNe Ia, the cosmological models are used to fit SN Ia distance moduli (μ) as a function of redshift (for example, see Riess et al. 1998; Perlmutter et al. 1999; Betoule et al. 2014; Scolnic et al. 2018; Abbott et al. 2019). However, as SN Ia samples grow larger, the variation in brightness between individual SNe no longer becomes the limiting issue. Instead, common systematics that change the effective average difference for large subsets of the sample become important. Photometric calibration and a proper treatment of PWV are thus keys in achieving the goals of large surveys such as LSST.

The importance of calibration in controlling cosmological uncertainties is well demonstrated in the literature. In the recent cosmological analysis of the Pantheon SN Ia sample (Scolnic et al. 2018), photometric calibration uncertainties contributed between 2 and 6 mmag, constituting up to half of the total uncertainty in cosmological parameters. Similarly, in Lasker et al. (2019), system transmission uncertainties introduced a redshift-dependent bias in SN Ia luminosity distances of ~ 0.02 mag. While we note in both cases that atmospheric effects were not considered separately from instrument throughput, we argue that variable atmospheric absorption can play a significant role in the z -band calibration uncertainties, particularly in thicker CCDs with increased sensitivities in the 940–980 nm water band.

The SEDs of SNe Ia are quantitatively different from those of stars. They have wide absorption lines characteristic of the elemental composition and $10,000 \text{ km s}^{-1}$ typical explosion speeds. SN Ia light-curve fitting uses this and models the spectrum of SN Ia as part of the forward modeling, but it needs

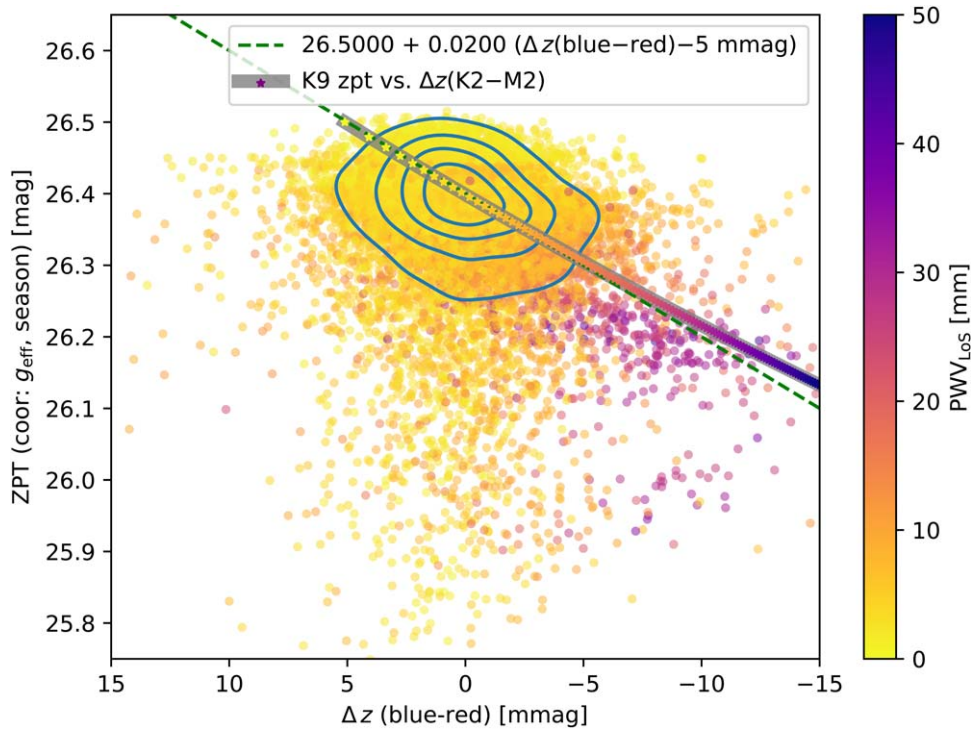


Figure 18. MzLS zero-point vs. Δz (blue – red), color-coded by PWV_{Los} . The contour lines enclose (20%, 40%, 60%, 80%) of the points. Green dashed line: a simple linear relationship explains the major axis of the contours. Gray line + stars color-coded by PWV_{Los} : a model of the expected zero-point change for a calibration based on a K9 star vs. the expected change in relative apparent brightness between K2–M2 star. The model curves up from the linear model as more water lines saturate—the M2 SED remains more sensitive to the increased PWV than the K2 or K9 SEDs. While the observed zero-point is in agreement with the stellar model (project the model PWV colors and the data colors onto the zero-point axis), the observed Δz (blue – red) data do not go as negative as expected by the model.

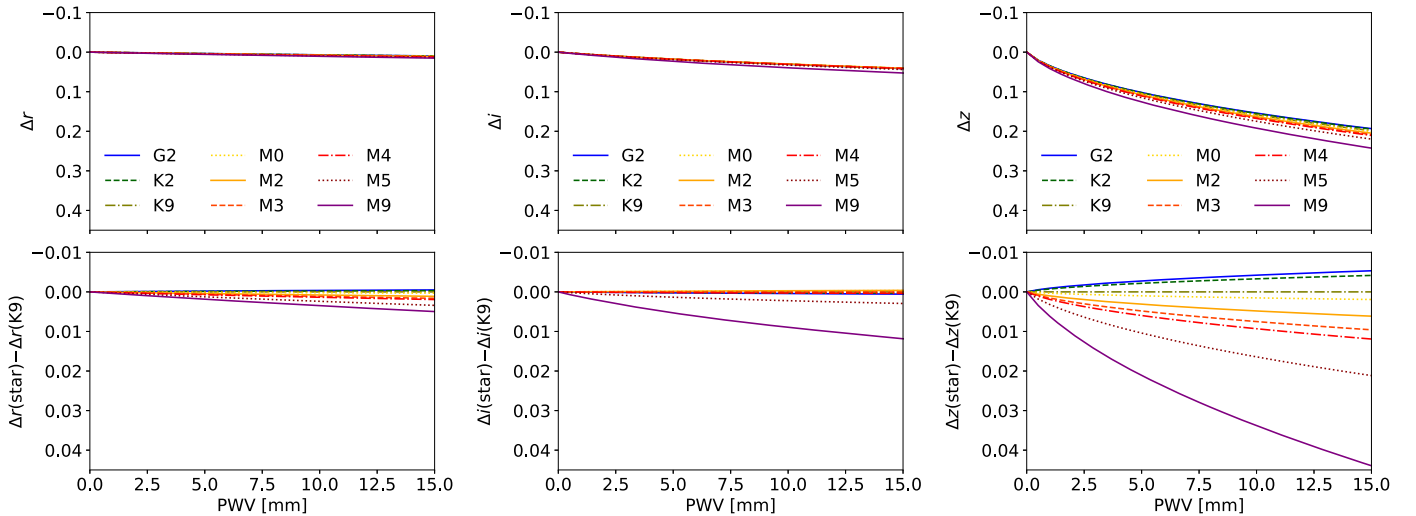


Figure 19. Change in stellar r -band (left), i -band (center), and z -band (right) photometry for G2, K2, K9, M0, M2, M3, M4, M5, and M9 stars (top) and the induced error from PWV assuming target–reference star combinations (bottom). The magnitude scale for the top panels is 10 times that of the bottom panels.

an accurate and precise transmission function to do so. Photometric calibration based on the stars in the image traditionally provides just a color term, which is the equivalent of a smooth variation of the transmission function. To precisely calibrate SNe Ia, the full transmission function needs to be determined, including the highly nonsmooth variation due to PWV absorption.

The complex structure of PWV absorption features is neither uniform nor constant. The variation in PWV absorption causes the apparent brightness of observed targets to vary as a function of redshift, as different features are redshifted across the water

absorption bands. This effect is most significant for high-redshift SNe Ia ($z \sim 1$) when the brightest region of the SED ($\lambda \approx 400$ nm) begins to enter the z and y bands (see Figure 21). However, even for low-redshift targets, the temporal variations in the atmospheric transmission function introduce a bias in the estimated color of SNe Ia.

To demonstrate how PWV absorption impacts photometric SNe Ia observations, we use the SALT2 spectroscopic template from Guy et al. (2007) to simulate sets of SN Ia light curves for a range of PWV values and over a redshift range of $0 \lesssim z \lesssim 1$. We assume a fixed PWV concentration for each set of SNe Ia.

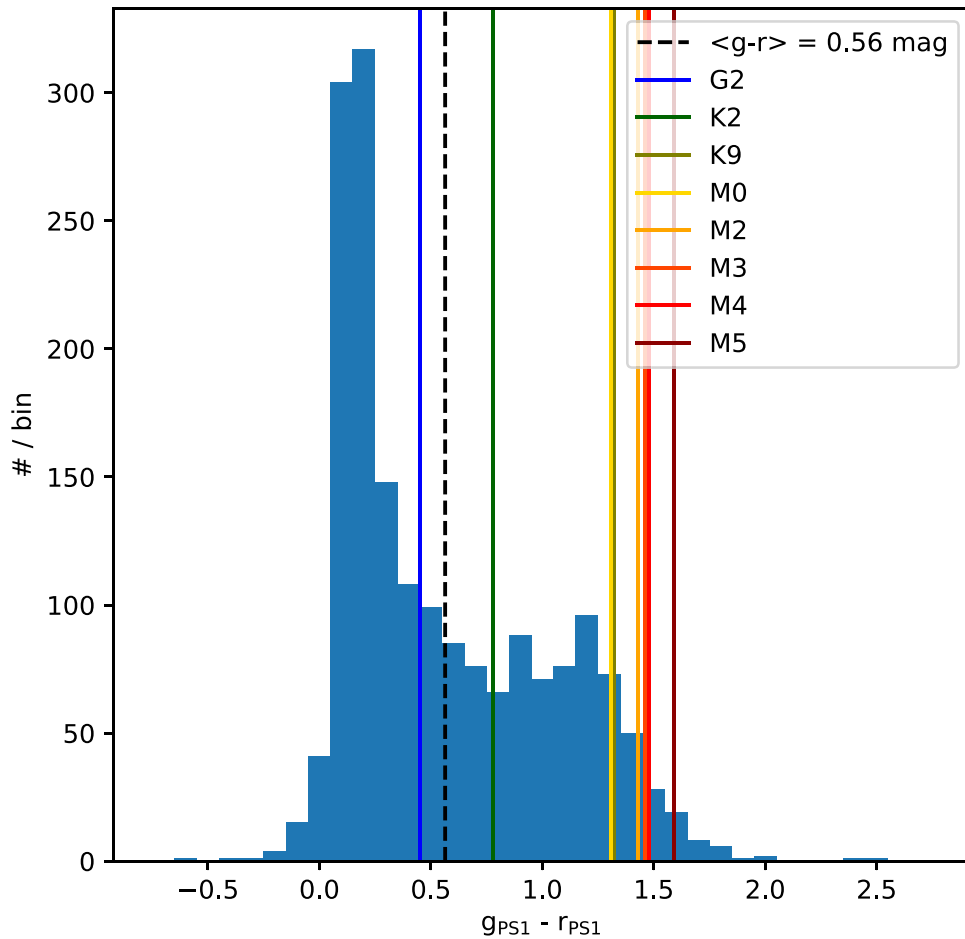


Figure 20. The $g - r$ color distribution of the PS1 reference catalog used for the MzLS calibration. Reference stars of different colors will be affected differently by varying PWV amounts. The mean color is between that of a K9 star and a K2 star. If one assumes that the calibration effectively takes an average over the mean color of the reference catalog, then the PWV effect should go approximately with the mean color of the reference stars.

The simulated light curves are then fit using the SALT2 model without a PWV component. For simplicity, we simulate SNe Ia having the fiducial model stretch ($x_1 = 1$) and color ($c = 0$). We also fix t_0 and z to the simulated values. We simulate a daily observational cadence in each of the $rizy$ bands. The supernova is thus sampled in a phase from $(-15-+50)/(1+z)$ days. The other SALT2 model parameters, x_0 , x_1 , and c , are left free with flat, independent priors.

Figure 22 shows the residuals in the distance moduli as determined from the simulated SNe. Note that this makes the unphysical assumption that PWV is constant for all points in the SN Ia light curve. In realistic conditions, PWV would vary and these biases would be averaged down. However, a season dependence of average PWV would translate into a bias as a function of R.A. as there is a correlation between average PWV and observed R.A. Even for relatively dry, photometric conditions ($\text{PWV} \lesssim 4$), uncorrected PWV absorption introduces a bias of up to 0.02 mag in the estimated μ . A similarly sized shift is also found for low-redshift targets suffering from PWV absorption that varies by more than a few mm away from the assumed fiducial atmospheric value. This is just another reminder that the assumption of a fiducial transmission model that is constant from image to image, such as when constructing the effective passband throughputs for a given survey, is not sufficient for achieving the millimag level of precision anticipated from future large-scale surveys.

We note that our results are similar in size to Hubble residuals found in existing cosmological analyses. For example, after assuming a mean atmospheric absorption model to calibrate instrumental magnitudes, the cosmological analysis of Betoule et al. (2014) found average residuals in the fitted μ of approximately 0.01 and 0.06 mag for their low- and high-redshift S/N samples respectively. Calibration uncertainties were the largest contributing factor in measurement uncertainty, and made up over 36% of the measurement uncertainty in Ω_m .

5.3. Quasars

The sample of known quasars has grown substantially in the last two decades thanks to surveys like SDSS, Pan-STARRS, and DES (Richards et al. 2009; Schindler et al. 2019; Tie et al. 2017). The current sample of over a million quasars is expected to grow tenfold with LSST (LSST Science Collaboration et al. 2009). With such a large sample, obtaining spectra will not be possible for all objects, and the photometrically derived redshifts will therefore remain important classifiers. Furthermore, sampling the temporal variability of quasars photometrically enables the study of the physical nature of these objects (Schmidt et al. 2011).

The SED of a typical quasar is marked by several prominent emission features including Lyman α in the UV and H α

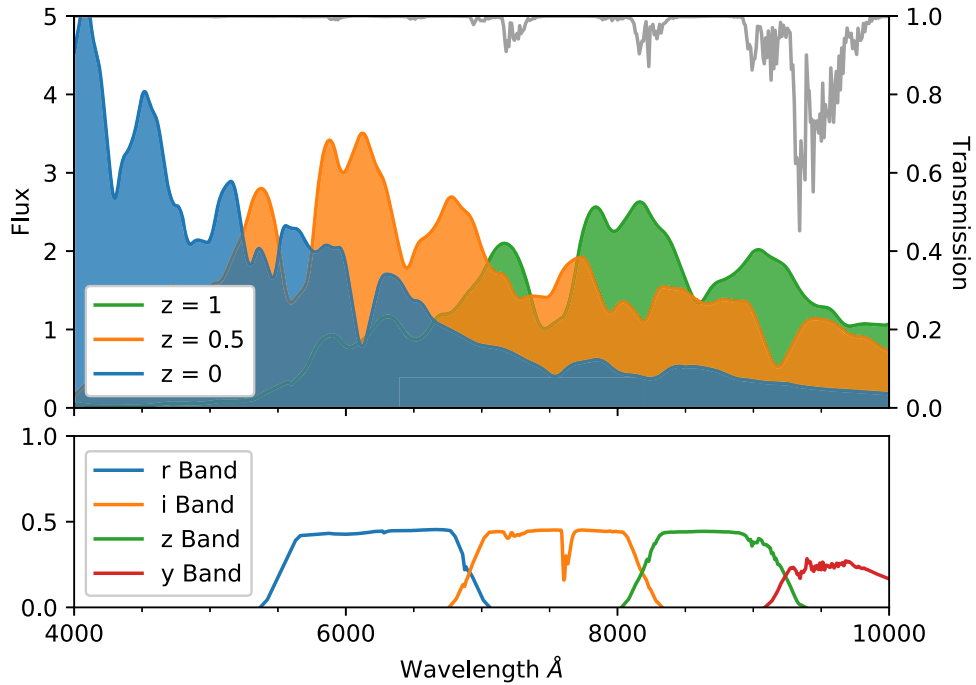


Figure 21. The spectral template of the Salt2 supernova model for a redshift of $z = 0$ (blue), 0.5 (orange), and 1 (green) against the PWV transmission (gray) for a PWV concentration of 4 mm. SN Ia spectra are dominated by several broad-absorption features, many of which have equivalent widths similar to the widths of PWV absorption features in the zy bands. As the template spectrum is shifted to higher redshifts, different spectral features begin to overlap with the strong PWV absorption feature at $\lambda \approx 950$ nm.

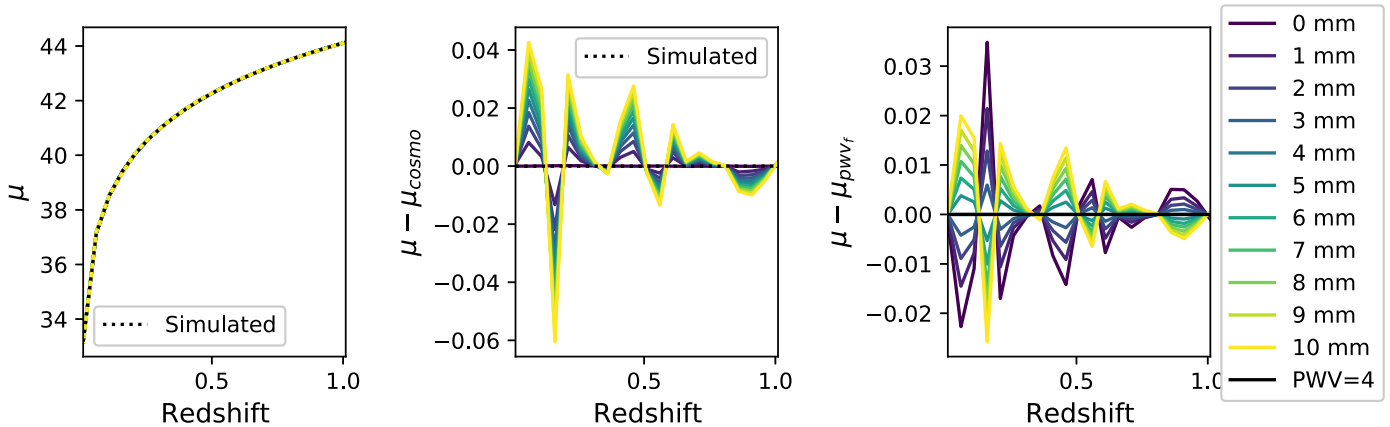


Figure 22. Distance modulus residuals ($\Delta\mu$) determined from a set of simulated SNe Ia, each suffering from a different level of PWV absorption (assumed constant for the full light curve). Residuals are shown both relative to the underlying cosmology of the simulation (center) and to a fiducial atmosphere of 4 mm PWV (right). The pattern with redshift comes from the broad features of SN Ia spectra moving across the water vapor absorption features.

emission at redder wavelengths. In Figure 23, we show how these and other prominent emission features shift with redshift causing them to overlap with absorption features due to water vapor in Earth’s atmosphere. Due to the large flux contribution by these emission features in a given photometric band, when the features align with Earth’s atmospheric absorption, there is the potential for a significant error in the zero-point correction that will be a function of the PWV during the observation.

To quantify the error in the photometry of a typical quasar spectrum, we use the composite quasar spectrum described in Berk et al. (2001). This spectrum was generated by averaging together over 2000 SDSS spectra to provide a high S/N spectrum that is characteristic of a typical quasar spectrum and covers a wide restframe wavelength range of 80 – 855 nm. Using the TAPAS telluric transmission spectrum and this

composite spectrum, we compute the change in magnitude in r , i , and z passbands and compare it to the extinction in a K9 reference star in the same atmospheric conditions. We compute this error term on a redshift grid ranging from 0.15 to 7 . The error in r is less than 1 mmag at all values of redshift and PWV considered, while the i and z bands have errors as high as ± 7 and ± 30 mmag, respectively, for the highest changes in PWV from nominal observing conditions, assumed to be 4 mm. Figure 24 shows the full effect for σ_i and σ_z as a function of redshift and PWV. As expected, the largest errors are observed when strong spectral features overlap with absorption in Earth’s atmosphere. Quasars at $z 0.4$ show large magnitude changes due to $H\alpha$ overlapping the strong 940 nm water vapor band. The same is true at $z > 6$ due to overlap of the $Ly\alpha$ with the same telluric water vapor band, which we note becomes

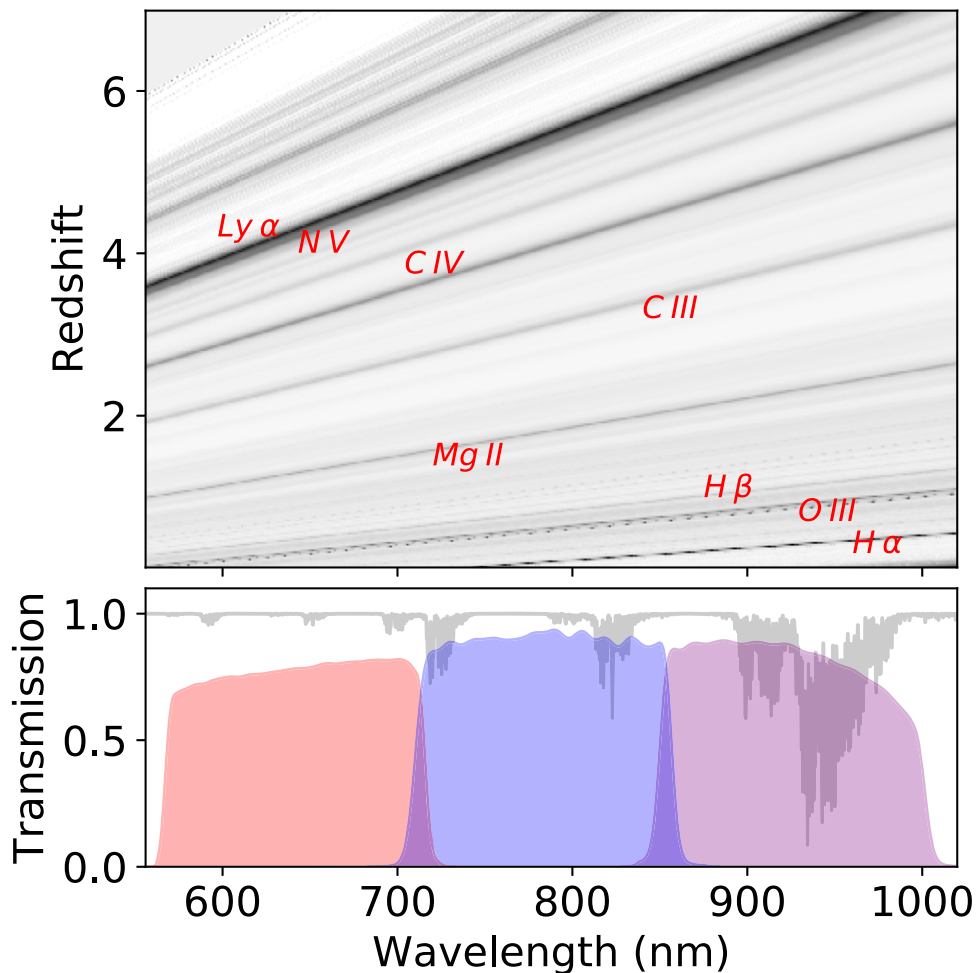


Figure 23. Top: quasar spectra at different redshifts with prominent emission lines. Bottom: telluric spectra and r , i , and z MzLS filter profiles.

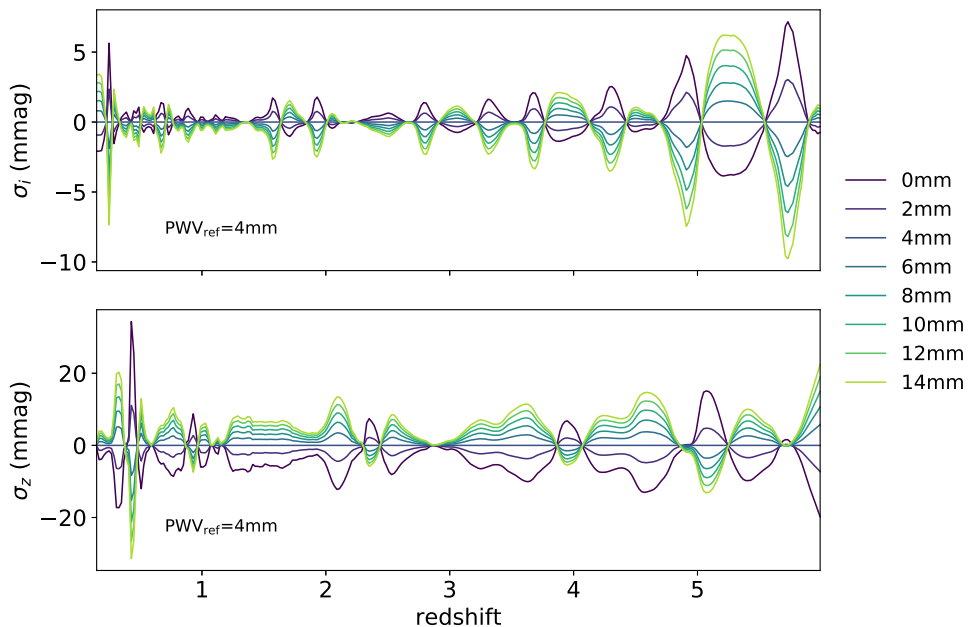


Figure 24. Error in the i band (top) and z band (bottom) of a composite quasar at various redshifts and PWV values. Errors are referenced to a nominal PWV value of 4 mm.

twice as large an effect when assuming a G2 reference star. We note that oxygen absorption was not considered here; however observations at a different airmass would also induce errors in

magnitude when prominent quasar spectral features overlap the oxygen-A and -B bands, which fall in the i , and r bands, respectively.

Quasars vary in brightness on timescales from hours to years (Ulrich et al. 1997; Vanden Berk et al. 2004; de Vries et al. 2005; Kimura et al. 2020). While 5–30 mmag changes in z magnitudes are quite small with respect to the long-term intrinsic variability of quasars, on short timescales, the PWV-induced variability can be greater than the short-term intrinsic variability of quasars. If the cadence of observations is high enough and the PWV during observations is known, this absorption could help constrain the redshift of an object. Other efforts to utilize the effects of Earth’s atmosphere to aid photometric redshift estimates include the works by Graham et al. (2018) and Kaczmarczik et al. (2009). In Kaczmarczik et al. (2009), the authors show how atmospheric refraction causes objects with different SEDs to experience different positional offsets, which can help break the degeneracies in photometric redshift estimates. The authors therefore suggest that surveys like LSST observe several frames of a part of the sky at high airmass to increase the magnitude of the differential chromatic refraction between survey objects. Graham et al. (2018) also show how higher-airmass observations can produce changes in an object’s magnitude that are a function of the object’s type. Since water vapor absorption is variable in time, looking for correlations between the z magnitudes (or LSST y) with PWV in time would further aid in breaking degeneracies.

The PWV-induced errors in quasar color may also be pertinent to studies monitoring the color variability of these objects. This added scatter in the r and z bands should be noted in such an analysis for quasars at redshifts that maximize the color error. Because quasars are prevalent throughout the sky, another use of this effect could be to generate a sample of quasars at redshifts leading to an overlap with prominent spectral features that can then be used to track changes in PWV. For this to work, many quasars would need to be monitored to average down their intrinsic variability in order to reveal their common-mode variability due to changing PWV. Wide-field surveys such as LSST may observe sufficient quasars in one exposure to identify the common-mode variability.

6. Discussion and Conclusions

We use independently measured PWV values from a dual-band GPS system to successfully model much of the zero-point sensitivity variation in the MzLS survey.

In principle, the effect of PWV should be determinable from the differential change in magnitude between stars of different spectral types. In practice, we found that PWV measurements from the dual-band GPS system at KPNO did a significantly better job of predicting z -band zero-point variation than using the differential change in the brightness of stars of different spectral types. Further more, the dual-band GPS-measured PWV allowed us to successfully correct the observed stellar-color-dependent errors along with explaining the nonsecular zero-point variations.

Despite its nonsmooth nature, PWV absorption can be reasonably well accounted for in a simple linear treatment for SEDs that are smooth. Specifically, the difference is very small for O–K stars because the SEDs of these stars are well approximated as smooth blackbodies, and the z band is on the Rayleigh–Jeans self-similar tail for these objects. However, the difference is noticeable for M dwarfs and more so for even cooler stars both because the SED becomes nonmonotonic within the z bandpass as the peak shifts through the bandpass

and because, as molecules start to form in the stellar atmosphere, the SED deviates noticeably from that of a blackbody. This difference has more significant consequences when observing objects with nonstellar SEDs across of range of redshifts, such as supernovae and quasars. In addition, for time-domain science with strict requirements on accuracy and precision, such as SN Ia cosmology or exoplanet characterization around M dwarfs, a dual-band GPS system can provide more precise measurements of PWV on a per-observation basis.

An ideal calibration system would utilize all four of the following complementary methods: (1) large-scale forward modeling of repeated visits; (2) narrowband imaging of stars; (3) contemporaneous stellar spectra; and (4) dual-band GPS measurements. Reliance on a single method is a high risk and will result in uncalibrated data when a method fails. Relying on just two methods means that you use one to calibrate and the second to check; what do you do when they disagree? Having three or more different methods available allows for a more robust determination with the ability to identify aberrations in any one particular method.

While we here used the SuomiNet processing of the data from KPNO, it is not necessary to use the SuomiNet system. The PWV calculation just requires the dual-band GPS time-delay measurement, the local pressure, the local relative humidity, and the temperature in the lower atmosphere. The first three are local measurements, while the last can be obtained from a weather model for the time and region.

The FGCM model used in DES Y3A1 calibration successfully took advantage of (1) and (4). Future DES calibrations should be able to add (2) using data from aTmCAM (Li et al. 2014) and provide a comparison of the two different auxiliary methods of determining PWV.

The list is not precisely parallel. While (2)–(4) are distinct methods with different instrumentation, (1) is an analysis approach: a forward-modeling approach can be used not just for the main survey science data, but could also make use of information from (2)–(4) by including those results as data that the forward model could either incorporate or seek to explain.

We recommend that astronomical observatories install and keep dual-band GPS monitoring systems at observatories. Large surveys may eventually have enough repeated measurements to calibrate out PWV absorption for the stellar population, and with a forward-modeling approach potentially for more general SEDs. But even the calibration of the DES Y3 data, which had ample multiepoch and multifilter data, was clearly improved by using independently measured PWV from auxiliary sources. Smaller programs, or single-pass surveys, are less able to make such corrections. A dual-band GPS system is inexpensive and provides specific and accurate information about the PWV impact on atmospheric transmission.

Our thanks to Dustin Lang, David Schegel, Arjun Dey, and the DECALS team for rapid and helpful responses to questions we had in the analysis of this data. Part of the catalyst for this paper was a conversation between M.W.-V. and D. Schlegel at the 20th Anniversary Subaru Meeting hosted by the NOAJ in Waikola, Hawai’i. Our thanks to the anonymous referee, whose comments improved this manuscript—particularly the suggestion to look more carefully at potential variation in the effective gain.

This work was supported in part by the US Department of Energy Office of Science under DE-SC0007914.

The Legacy Surveys consist of three individual and complementary projects: the Dark Energy Camera Legacy Survey (DECaLS; NOAO Proposal ID # 2014B-0404; PIs: David Schlegel and Arjun Dey), the Beijing-Arizona Sky Survey (BASS; NOAO Proposal ID # 2015A-0801; PIs: Zhou Xu and Xiaohui Fan), and the Mayall z -band Legacy Survey (MzLS; NOAO Proposal ID # 2016A-0453; PI: Arjun Dey). DECaLS, BASS, and MzLS together include data obtained, respectively, at the Blanco telescope, Cerro Tololo Inter-American Observatory, National Optical Astronomy Observatory (NOAO); the Bok telescope, Steward Observatory, University of Arizona; and the Mayall telescope, Kitt Peak National Observatory, NOAO. The Legacy Surveys project is honored to be permitted to conduct astronomical research on Iolkam Du'ag (Kitt Peak), a mountain with particular significance to the Tohono O'odham Nation.

This work is based in part on observations taken at Kitt Peak National Observatory, National Optical Astronomy Observatory, which is operated by the Association of Universities for Research in Astronomy (AURA) under a cooperative agreement with the National Science Foundation.

Appendix CCD Temperature Variation Was Not a Source of Significant Zero-point Variation

Variations in CCD temperatures could potentially have a significant effect on the z -band quantum efficiency (QE). We here look in more detail at potential correlations between CCD temperatures for the z -band variations from MzLS. As the incident photon wavelengths approach the Si band-gap energy ($\lambda \sim 1100$ nm), single- and double-phonon-assisted conversion of photons becomes at first a significant source and then the dominant source of the promotion of electrons into the conductance band.

One distinction for the z -band filters for Mosaic3, DECam, and LSSTCam is that they explicitly cut off at $\lambda = 1000$ nm. This is in contrast to the original SDSS z -band filter, which had no red cutoff, and it was the CCD response that determined the response on the red side of the passband. This explicit cutoff 100 nm away from the Si band-gap cutoff substantially reduces the temperature sensitivity of z -band observations.

In addition to the filter design, the thickness of the CCD matters. Thicker CCDs have more opportunities for absorption of the incoming photon than thinner CCDs at the same temperature, and the effective absorption length is an

decreasing function of temperature. Groom et al. (2017) provide a detailed discussion of the transmissions for thick CCD sensors and compare measured data to theoretical models of transmission. Figure 2 of Groom et al. (2017) shows the absorption length is $\sim 200 \mu\text{m}$ at $\lambda = 1000$ nm, following the models of Rajkanan et al. (1979).

In an analysis of the $500 \mu\text{m}$ thick LBNL CCDs used for Mosaic3 and DECam, Diehl et al. (2008) found a $\frac{1}{\text{QE}} \frac{d\text{QE}}{dT} = (0.0001, 0.002, 0.004) \text{ C}^{-1}$ fractional change in QE at $\lambda = (900, 950, 1000)$ nm from -110 to -90 C. The equivalent change in mmag can be computed as $(2.5 \log_{10} e) \frac{\Delta\text{QE}}{\text{QE}} = (0.11, 2.2, 4.3) \text{ mmag C}^{-1}$. One should integrate over the passband to get the full change, but these monochromatic numbers are helpful in estimating the size of the effect. Tonry et al. (2012) found a similar 0.003 C^{-1} fractional change in QE at $\lambda = 1000$ nm at a warmer -83 C for the $75 \mu\text{m}$ thick CCDs for Pan-STARRS1 survey.

O'Connor (2019) measured sensitivity parameters for the assembled raft tower modules for the LSST Camera, which uses $100 \mu\text{m}$ thick deep depletion CCDs from two different vendors: E2V and ITL. This analysis found a z -band fractional QE temperature coefficient of $(0.00088, 0.00063) \text{ C}^{-1}$ from measurements at -90 C and -100 C for the (E2V, ITL) detectors. These coefficients translate to a change in zero-point sensitivity of $(0.96, 0.68) \text{ mmag C}^{-1}$. For comparison the same coefficients for y are 5–10 times greater at $(0.51\%, 0.80\%) \text{ C}^{-1}$, or $(5.5, 8.7) \text{ mmag C}^{-1}$.

Figure 25 shows the CCD temperatures for the Mosaic3 camera over the course of the MzLS survey. Each CCD stayed within 2 C of its typical temperature over the course of the MzLS survey (see Table 5), with the exception of 6 outlier nights. We compiled these data by extracting the CCDTEMP1,2,3,4 values from the FITS file headers of the files on disk at NERSC.

There are six nights in the survey where the CCD temperatures were significant outliers. See Table 6. There is one night when the CCD temperatures were at < -125 C. There are five more nights when the CCD temperatures were at < -110 C. There is no significant zero-point dependency detectable on these nights; it does not noticeably affect the variance of (gain, PWV) corrected zero-point. If we just take the $\lambda = 950$ nm temperature coefficient from the Diehl et al. (2008) measurements, we would expect a 4.4 mmag change in zero-point from a 2 C change in temperature. We thus attribute < 5 mmag of zero-point variation to be due to CCD temperature changes.

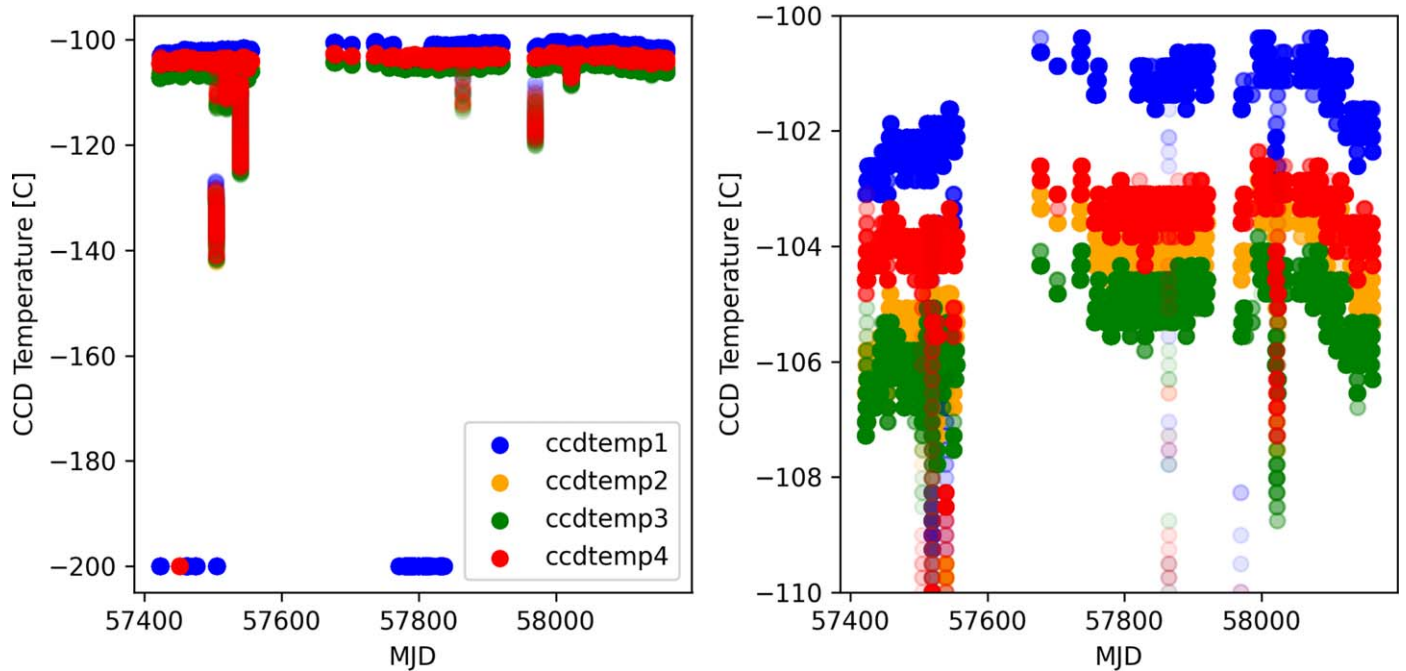


Figure 25. The CCD temperatures over the two years of the survey. Variation was about 2 C for each CCD, and each CCD had an ~ 1 C offset with respect to the other CCDs. Left: full temperature range—note the 6 outlier nights (the first two nights appear together on this plot). We interpret the recorded values at -200 C as anomalous. Right: zoom on the typical range during the survey. The discreteness in the temperature measurements is due to a 0.246 C step size in the digitization of the signal.

Table 5
MzLS CCD Temperatures

CCD	Median Temperature (C)	NMAD ^a (C)	Standard Deviation (C)
1	-101.38	1.10	2.00
2	-104.33	1.10	2.05
3	-105.32	0.73	1.91
4	-103.59	0.73	5.43

Note.

^a The CCD temperatures are discretized in steps of 0.246 C, which makes the median absolute deviation discrete, and leads to the two-significant figure agreement between CCD1 + 2 and CCDs3 + 4. We include the NMADs primarily to indicate that the large value of the CCD4 standard deviation is due to outliers.

Table 6
MzLS CCD Temperature Outlier Nights

Observing Night (MST) ^a	MJD	T (C)
2016-04-25	57,504	-125–142
2016-04-26	57,505	-110–112
2016-05-10	57,519	-110–125
2016-05-30	57,539	-110–112
2017-04-20	57,864	-110–112
2017-08-03	57,969	-110–120

Note.

^a UTC is 6 hr ahead of MST, and the observing nights are defined by the local date at the start of the evening, so the MJDs above are for the next UTC dates.

ORCID iDs

W. M. Wood-Vasey  <https://orcid.org/0000-0001-7113-1233>
 Daniel Perrefort  <https://orcid.org/0000-0002-3988-4881>
 Ashley D. Baker  <https://orcid.org/0000-0002-6525-7013>

References

- Abbott, T. M. C., Allam, S., Andersen, P., et al. 2019, *ApJL*, 872, L30
 Baker, A. D., Blake, C. H., & Sliski, D. H. 2017, *PASP*, 129, 85002
 Berk, D. E. V., Richards, G. T., Bauer, A., et al. 2001, *AJ*, 122, 549
 Bertaux, J. L., Lallement, R., Ferron, S., Boonne, C., & Bodichon, R. 2014, *A&A*, 564, A46
 Betoule, M., Kessler, R., Guy, J., et al. 2014, *A&A*, 568, A22
 Bevis, M., Businger, S., Chiswell, S., et al. 1994, *JApMe*, 33, 379
 Bevis, M., Businger, S., Herring, T. A., et al. 1992, *JGRD*, 97, 15787
 Blake, C. H., & Shaw, M. M. 2011, *PASP*, 123, 1302
 Brault, J. W., Fender, J. S., & Hall, D. N. 1975, *JQSRT*, 15, 549
 Braun, J., & Hove, T. 2005, in Proc. of the 18th Int. Technical Meeting of the Satellite Division of The Institute of Navigation, ed. Christian Rocken & Ted Iwabuchi (Long Beach, CA: Institute of Navigation), <http://n2t.net/ark:/85065/d7639nsm>
 Buehler, S. A., Östman, S., Melsheimer, C., et al. 2012, *ACP*, 12, 10925
 Burke, D. L., Axelrod, T., Blondin, S., et al. 2010, *ApJ*, 720, 811
 Burke, D. L., Rykoff, E. S., Allam, S., et al. 2018, *AJ*, 155, 41
 Burke, D. L., Saha, A., Claver, J., et al. 2014, *AJ*, 147, 19
 Burleigh, K. J., Landriau, M., Dey, A., et al. 2020, *AJ*, 160, 61
 Dark Energy Survey Collaboration, Abbott, T., Abdalla, F. B., et al. 2016, *MNRAS*, 460, 1270
 de Vries, W. H., Becker, R. H., White, R. L., & Loomis, C. 2005, *AJ*, 129, 615
 Dey, A., Rabinowitz, D., Karcher, A., et al. 2016, *Proc. SPIE*, 9908, 99082C
 Dey, A., Schlegel, D. J., Lang, D., et al. 2019, *AJ*, 157, 168
 Dey, A., & Valdes, F. 2014, *PASP*, 126, 296
 Diehl, H. T., Angstadt, R., Campa, J., et al. 2008, *Proc SPIE*, 7021, 702107
 Dumont, D. M., & Zabransky, J. 2001, in Proc. of the Eleventh Symp. on Meteorological Observations and Instrumentation (Boston, MA: AMS), 245
 Flaugher, B., Diehl, H. T., Honscheid, K., et al. 2015, *AJ*, 150, 150
 Graham, M. L., Connolly, A. J., Ivezić, Ž., et al. 2018, *AJ*, 155, 1
 Groom, D. E., Haque, S., Holland, S. E., & Kolbe, W. F. 2017, *JAP*, 122, 055301
 Guy, J., Astier, P., Baumont, S., et al. 2007, *A&A*, 466, 11
 Hagemann, S., Bengtsson, L., & Gendt, G. 2003, *JGRD*, 108, D21
 Husser, T. O., Wende-von Berg, S., Dreizler, S., et al. 2013, *A&A*, 553, A6
 Ivezić, Ž., Kahn, S. M., Tyson, J. A., et al. 2019, *ApJ*, 873, 111
 Ivezić, Ž., Smith, J. A., Miknaitis, G., et al. 2007, *AJ*, 134, 973
 Kaczmarczik, M. C., Richards, G. T., Mehta, S. S., & Schlegel, D. J. 2009, *AJ*, 138, 19
 Kimura, Y., Yamada, T., Kokubo, M., et al. 2020, *ApJ*, 894, 24
 Lasker, J., Kessler, R., Scolnic, D., et al. 2019, *MNRAS*, 485, 5329
 Li, D., Blake, C. H., Nidever, D., & Halverson, S. P. 2017, *PASP*, 130, 14501
 Li, T., DePoy, D. L., Marshall, J. L., et al. 2014, *Proc. SPIE*, 9147, 91476Z
 Li, T. S., DePoy, D. L., Marshall, J. L., et al. 2016, *AJ*, 151, 157
 LSST Science Collaboration, Abell, P. A., Allison, J., et al. 2009, [arXiv:0912.0201](https://arxiv.org/abs/0912.0201)
 Magnier, E. A., Schlafly, E. F., Finkbeiner, D. P., et al. 2020, *ApJS*, 251, 6
 Manandhar, S., Lee, Y. H., Meng, Y. S., Yuan, F., & Dev, S. 2018, [arXiv:1805.01961](https://arxiv.org/abs/1805.01961)
 Moore, A. W., Small, I. J., Gutman, S. I., et al. 2015, *BAMS*, 96, 1867
 Nahmias, M. H., & Zabransky, J. 2004, *BAMS*, 2004, P1.7
 O'Connor, P. 2019, *JATIS*, 5, 041508
 Perlmutter, S., Aldering, G., Goldhaber, G., et al. 1999, *ApJ*, 517, 565
 Perrefort, D., Wood-Vasey, W. M., Bostroem, K. A., et al. 2019, *PASP*, 131, 25002
 Rajkanan, K., Singh, R., & Shewchun, J. 1979, *SSEle*, 22, 793
 Richards, G. T., Myers, A. D., Gray, A. G., et al. 2009, *ApJS*, 180, 67
 Riess, A. G., Filippenko, A. V., Challis, P., et al. 1998, *AJ*, 116, 1009
 Sapucci, L. F., Machado, L. A. T., de Souza, E. M., & Campos, T. B. 2019, *MeApp*, 26, 49
 Schindler, J.-T., Fan, X., Huang, Y.-H., et al. 2019, *ApJS*, 243, 5
 Schlafly, E., Finkbeiner, D. P., & Juric, M. 2012, AAS Meeting Abstracts, 219, 428.16
 Schmidt, K. B., Rix, H.-W., Shields, J. C., et al. 2011, *ApJ*, 744, 147
 Scolnic, D. M., Jones, D. O., Rest, A., et al. 2018, *ApJ*, 859, 101
 Shangguan, M., Heise, S., Bender, M., et al. 2015, *AnGeo*, 33, 55
 Stubbs, C. W., High, F. W., George, M. R., et al. 2007, *PASP*, 119, 1163
 Thomas-Osip, J., McWilliam, A., Phillips, M., et al. 2007, *PASP*, 119, 697
 Thomas-Osip, J. E., Prieto, G., McWilliam, A., et al. 2010, *Proc. SPIE*, 7733, 77334N
 Tie, S. S., Martini, P., Mudd, D., et al. 2017, *AJ*, 153, 107
 Tonry, J. L., Stubbs, C. W., Lykke, K. R., et al. 2012, *ApJ*, 750, 99
 Tralli, D. M., & Lichten, S. M. 1990, *BGeod*, 64, 127
 Ulrich, M.-H., Maraschi, L., & Urry, C. M. 1997, *ARA&A*, 35, 445
 Vanden Berk, D. E., Willite, B. C., Kron, R. G., et al. 2004, *ApJ*, 601, 692
 Wade, R. A., & Horne, K. 1988, *ApJ*, 324, 411
 Ware, R. H., Fulker, D. W., Stein, S. A., et al. 2000, *BAMS*, 81, 677